JAMES | Journal of Advances in Modeling Earth Systems

RESEARCH ARTICLE
10.1029/2024MS004735

Impact of Ice Topography, Basal Channels and Subglacial Discharge on Basal Melting Under the Floating Ice Tongue of 79N Glacier, Northeast Greenland

Mahdi Mohammadi-Aragh[1,2], Ole Zeising[2], Markus Reinert[1,3], Knut Klingbeil[1], Angelika Humbert[2,4], Rebecca McPherson[2], Mathieu Morlighem[5], Ralph Timmermann[2], Claudia Wekerle[2], and Hans Burchard[1]

[1]Leibniz Institute for Baltic Sea Research Warnemünde (IOW), Rostock, Germany, [2]Alfred Wegener Institute (AWI) Helmholtz Centre for Polar and Marine Research, Bremerhaven, Germany, [3]Federal Waterways Engineering and Research Institute, Hamburg, Germany, [4]Faculty of Geosciences, University of Bremen, Bremen, Germany, [5]Department of Earth Sciences, Dartmouth College, Hanover, NH, USA

Key Points:

- Basal channels regulate the melt rate of 79N Glacier, making their modeling crucial for estimating the melt rate of ice shelves influenced by warm water
- A new drying and flooding algorithm solves the issue of plume water velocity divergence
- Subglacial discharge primarily affects melt rate in the hinge zone, with minimal variation in the calving zone

Correspondence to:

M. Mohammadi-Aragh and C. Wekerle,
gipm.dvl@gmail.com;
claudia.wekerle@awi.de

Citation:

Mohammadi-Aragh, M., Zeising, O., Reinert, M., Klingbeil, K., Humbert, A., McPherson, R., et al. (2025). Impact of ice topography, basal channels and subglacial discharge on basal melting under the floating ice tongue of 79N Glacier, northeast Greenland. *Journal of Advances in Modeling Earth Systems*, *17*, e2024MS004735. https://doi.org/10.1029/2024MS004735

Received 25 SEP 2024
Accepted 17 JUL 2025

Author Contributions:

Conceptualization: Mahdi Mohammadi-Aragh, Angelika Humbert, Hans Burchard
Formal analysis: Mahdi Mohammadi-Aragh
Funding acquisition: Hans Burchard
Investigation: Mahdi Mohammadi-Aragh, Ole Zeising, Markus Reinert, Hans Burchard
Methodology: Mahdi Mohammadi-Aragh, Ole Zeising, Markus Reinert, Knut Klingbeil, Angelika Humbert, Rebecca McPherson, Ralph Timmermann, Hans Burchard
Resources: Hans Burchard
Software: Mahdi Mohammadi-Aragh, Hans Burchard
Supervision: Hans Burchard

Abstract The floating ice tongue of the 79N Glacier in Northeast Greenland has been thinning over the past two decades, with warning signs of a potential onset of disintegration. While previous studies primarily attribute the thinning of the ice shelf to oceanic heat flux, limited attention has been given to the significant role of ice shelf plume dynamics as a mechanism for distributing the heat beneath the ice shelf. Here, we develop a horizontal two-dimensional plume model to assess the effects of key factors influencing plume dynamics and, consequently, the estimation of a high-resolution basal melt rate. We examine the effect of ice basal topography roughness and the presence of basal channels, that is extreme roughness of the base in the hinge zone, as well as the impact and pathways of subglacial discharge on melt rates. Our model results show good agreement with observation-based melt rate estimates and indicate that basal channels in the hinge zone are the dominant control on the ice shelf's basal melt rates. In combination with subglacial discharge, the melt rate is increased to 150 m yr^{-1} at the grounding line, intensifying the channelized melt rate pattern created by basal channels and increasing spatial variability. Additionally, our results indicate that incorporating wet-dry algorithms and calculating a variable drag coefficient are crucial for accurately estimating melt rates during low subglacial discharge season, as well as for determining friction and turbulent exchange coefficients.

Plain Language Summary Ice shelves are floating extensions of polar ice sheets, and control how fast glaciers flow into the ocean. Many of them are rapidly thinning, primarily due to basal melting, thereby reducing their ability to slow down ice flow. Accurately estimating basal melt rates improves the reliability of sea level predictions. However, existing modeling efforts have predominantly focused on large-scale processes. This study employs a suite of simulations to investigate the role of narrow basal channels under the ice and the effect of freshwater discharge where the ice starts to float. Our sensitivity analysis focuses on the floating ice tongue of the 79N Glacier, in northeast Greenland, which has been experiencing thinning over the past few decades. The results highlight that narrow basal channels significantly increase both the variability and spatial mean melt rates where the ice starts to float, further amplified by subglacial discharge near the grounding line.

1. Introduction

Basal melting plays a key role in the interaction between ice sheets and oceanic processes by weakening ice shelves. This influences the buttressing of continental ice flux (Lilien et al., 2019) and regulates the retreat of outlet glaciers and large-scale ice streams (Walker et al., 2008), thereby controlling both ice mass balance and the contribution of the ice sheets to sea level rise (Hoffman et al., 2019; Purich, 2022). Changes in basal melting therefore poses significant risks to ice shelf integrity (K. E. Alley et al., 2019; Vaughan et al., 2012). Despite the considerable need for an accurate estimation of basal melt rates beneath ice shelves, this remains challenging due to the insufficient representation of physical processes in numerical models, significant uncertainties in ice thickness data sets, and limited in situ observations at the ice-ocean interface.

Our study focuses on the floating ice tongue of the 79N Glacier (referred to hereafter as 79NG), which has recently attracted significant attention across atmosphere-land and ice-ocean fields (Kanzow et al., 2025). Since 2001, 79NG has been out of equilibrium, undergoing substantial thinning (Mayer et al., 2018; Zeising

Validation: Mahdi Mohammadi-Aragh, Ole Zeising, Markus Reinert, Angelika Humbert, Mathieu Morlighem, Ralph Timmermann, Claudia Wekerle, Hans Burchard
Visualization: Mahdi Mohammadi-Aragh
Writing – original draft: Mahdi Mohammadi-Aragh
Writing – review & editing: Mahdi Mohammadi-Aragh, Ole Zeising, Markus Reinert, Knut Klingbeil, Angelika Humbert, Rebecca McPherson, Mathieu Morlighem, Ralph Timmermann, Claudia Wekerle, Hans Burchard

et al., 2024), and showing concerning signs of major changes at its eastern calving front, indicating the potential onset of disintegration (Humbert et al., 2023). Despite numerous studies attributing the observed thinning and basal melting of 79NG to heat flux from ocean warming (Lindeman et al., 2020; Mayer et al., 2018; McPherson et al., 2024; Schaffer et al., 2017, 2020; Wekerle et al., 2024; Wilson & Straneo, 2015; Wilson et al., 2017), exploration of ice shelf plume dynamics, the buoyancy-driven transport and downstream modification of the meltwater, and their role in basal melting remains limited.

This study aims to quantify the drivers of basal melt rate, namely (a) spatial variation of ice base topography, (b) ice shelf basal channels, that is, extreme roughness of ice base topography, and (c) the intensity, temperature and spatial distribution of subglacial discharge. To achieve our objectives, we conduct a series of numerical experiments incorporating various subglacial discharge scenarios and ice base topographies with different levels of smoothness. Additionally, we design an experiment using an ice base topography that includes basal channels in the hinge zone. While our study examines the influence of basal channels and spatial variation of ice base topography on basal melt rate, these two aspects are interconnected within the same spatial scale spectrum. The distinction between them is important for clarity, but they are not entirely separate, as they represent different scale classes of the same underlying surface. We also capture the influence of processes across these spatial scales, as demonstrated by our presentation of the Local Variation of Topography (LVT).

In the context of this study, we employ a prognostic approach and develop a new two-dimensional horizontal plume model called the General Ice Shelf Water Plume Model (GIPM; Mohammadi-Aragh & Burchard, 2024). GIPM sets itself apart from previous two dimensional plume models in a number of ways. These include integrating subglacial discharge as input boundary flux, introducing drying and flooding algorithms to tackle the issue of plume water velocity divergence as explained in Section 2.5, and incorporating a variable drag coefficient and variable heat and salt exchange velocities. The importance of tuning these variables was highlighted by Jenkins et al. (2010), as it reduces uncertainties in estimating turbulent transfer across the oceanic boundary layer between plume water and ice. Following the approach of Burchard et al. (2022), who applied a variable drag coefficient based on the logarithmic law of the wall, we incorporate this method in our modeling.

This paper is divided into seven sections. The second section offers essential background on plume modeling, basal melt rate approximation, and the associated challenges. It also explores the role of basal channels in melting and discusses factors influencing melt rate such as subglacial discharge, specifically tailored for 79NG. The third section explains the plume model (GIPM) and its characteristics. The fourth section covers the data and methodology. The fifth section presents the research findings, focusing on three key topics of sensitivity analysis. The following section discusses the results, offering new insights into the melt rate of 79NG. Finally, we summarize the general conclusions derived from the study.

Throughout this paper, we classify local melt rates as follows: rates above 100 m yr^{-1} are classified as extreme, rates between 60 and 100 m yr^{-1} are considered high, rates between 20 and 60 m yr^{-1} are considered moderate, and weaker rates are categorized as low. Note that these terms are used for clarity and specific to this particular ice shelf.

2. Background

2.1. Ice Shelf Basal Channels

Many recent studies have explored melting in basal channels, and how it can lead to fractures in ice shelves (K. E. Alley et al., 2016; Dow et al., 2018; Larter, 2022). These channels, whether ocean-sourced, subglacially-sourced, or grounding line sourced (K. E. Alley et al., 2016) have been found to positively correlate with basal melt rates, host ice-shelf meltwater (Chartrand et al., 2024; Rignot & Steffen, 2008) and lead to basal shelf erosion (Larter, 2022; Rignot & Steffen, 2008). Warm ocean water intrusion along these channels intensifies melt rates. Eroding channels can reach considerable heights, thereby reducing hydrostatic support for overlying ice (Le Brocq et al., 2013; Vaughan et al., 2012). The role of basal channel networks has already been observed and highlighted for various ice shelves such as Totten Glacier Ice Shelf, Petermann Glacier, Pine Island Glacier, Fimbulisen and Filchner Ice Shelf (Dow et al., 2018). The basal channels of 79NG have received less attention. However, when approximating basal melt rates, Zeising et al. (2024) have reported the growth of deep subglacial channels associated with significant surface lowering and a heterogeneous distribution of extreme melt rates in "hinge zone" that is, the area near the grounding line in which the ice is bent by tides. Additionally, Narkevic

et al. (2023) reported notable thinning of ice downstream of the 79NG grounding line in across ice flow oriented channels.

2.2. Subglacial Discharge, Hydraulically Efficient, and Dispersed Systems

Recent studies suggest that subglacial discharge increases localized (Nakayama et al., 2021) or spatial mean melt rate (Cai et al., 2017; Washam et al., 2019; Wekerle et al., 2024) by enhancing entrainment, that is, enhancing the transfer of oceanic heat under ice shelves (Jenkins, 2011; Washam et al., 2019). Subglacial discharge forms from meltwater at the ice-bed interface as a result of drained surface meltwater (supraglacial input) or from locally generated basal meltwater (Nienow et al., 2017). Supraglacial meltwater, which is transported through the ice, is seasonal and can be diagnosed by monitoring the ice speed in the hinge zone, as suggested by Sugiyama et al. (2011) and Vijay et al. (2019). The seasonal evolution of the spatial structure of the subglacial drainage system, as reviewed by Nienow et al. (2017), initially occurs through a dispersed system with limited hydraulic efficiency early in the melt season. As ice surface melting intensifies, increased water inputs destabilize components of this dispersed system, leading to channel formation, and form hydraulically efficient systems. These channels evolve into a branching network that extends up-glacier as connections to the glacier bed are established. While surface meltwater fluxes decrease toward the end of summer (Nienow et al., 2017), subglacial discharge does not necessarily shut down since local meltwater, due to geothermal and frictional melting, has the potential to contribute, although in a less dominant role. Neckel et al. (2020) revealed that 79NG shows a direct and strong correspondence between ice velocity and meltwater availability, suggesting that the development of an efficient basal drainage system is limited. Neckel et al. (2020) also showed that sudden supraglacial lake drainage of the 79NG was not routed through established channels but overwhelmed the subglacial hydraulic system.

2.3. Methodologies for Approximating Basal Melt Rates

A variety of methodologies have emerged to approximate the spatial distribution of basal melt rates of ice shelves, broadly classified into two approaches: diagnostic methods and prognostic models.

Diagnostic methods as outlined by Seroussi et al. (2011) and Dutrieux et al. (2013) aim to estimate basal melt rates using various observational data sets and numerical models. Satellite remote sensing imagery can resolve spatial patterns of basal melt rates on kilometer scales. These methods are not able to resolve melt rates in deep, narrow basal channels or the hinge zone, where the ice is not freely floating. The limitation arises from the reliance on the hydrostatic equilibrium assumption sufficiently away from grounded ice, which is valid for ice shelves with very high aspect ratios between horizontal length scale and ice thickness (Weertman, 1957). Ground-based radar measurements can overcome these limitations, but they are spatially limited. While in situ measurements can help refine estimates, their localized nature may not be suitable for comparisons on larger scales (Chartrand & Howat, 2023).

Prognostic models face challenges in accurately approximating basal melt rates, necessitating the validation of equations, careful selection of appropriate numerical methods, and incorporation of sparse spatiotemporal measured data as boundary and initial conditions. While studies are advancing in the application of turbulence models to estimate the basal melt rate for idealized studies (Anselin et al., 2024; Gayen et al., 2015; Zhao et al., 2024), ongoing research aims to narrow the persisting gaps in realistic modeling (Asay-Davis et al., 2017; Dinniman et al., 2016; Malyarenko et al., 2020) and constrain unknown parameters (Burchard et al., 2022; Gwyther et al., 2015; Losch, 2008; Zalesny & Ivchenko, 2010), collectively enhancing trust in the model outcomes. These gaps and associated possible remedy options have been discussed by R. B. Alley et al. (2015), Scambos et al. (2017), and further reviewed by Asay-Davis et al. (2017).

2.4. Approximation of the Basal Melt Rate of 79NG

Previous studies have provided melt rate estimates for 79NG. Using remote-sensing between 2011 and 2015, Wilson et al. (2017) inferred spatially heterogeneous basal melt rates with a mean of 8.2 m yr^{-1} and a maximum of 57 m yr^{-1}. G. Wang et al. (2024), also based on remote sensing data and a mass conservation approach, estimated mean melt rates of 7.98 m yr^{-1} for the time period 2013–2022. Millan et al. (2023) found a strong change in basal melt rates close to the grounding line, increasing from 21.1 m yr^{-1} in 2006–2011 to 29.0 m yr^{-1} in 2020. Anhaus (2017) and Mayer et al. (2018) used a one-dimensional plume model (Jenkins, 1991) to estimate

mean basal melting along several flowlines (transects). They concluded that the maximum magnitude of basal melting is reached close to the grounding line and decays toward the calving front, while Anhaus (2017) demonstrated a significantly higher melt rate along the flowline at the southern margin of the ice shelf compared to the northern margin. Mayer et al. (2018) estimated the mean melt rate as 8.7 ± 1.1 m yr^{-1} for the year 1998 and 12.2 ± 1.6 m yr^{-1} for the year 2014. Reinert et al. (2023) used a 2D-vertical slice model deploying adaptive vertical coordinates to compute the basal melt rate along a single transect in the center of the ice shelf, and found a mean basal melt rate of 12.3 m yr^{-1} and a maximum melt rate of 60 m yr^{-1} about 2 km downstream of the grounding line.

Using a high-resolution, three-dimensional ocean model with a minimum horizontal grid spacing of 700 m—which is still coarse to resolve small-scale features of the ice base—Wekerle et al. (2024) investigated ocean circulation beneath the ice shelf. They provided an estimate of 10.6 ± 4.9 m yr^{-1} for the year 2015. Their conclusions, supported later by McPherson et al. (2024), further highlighted that warming of the oceanic inflow has significantly contributed to basal melting over the past 50 years.

Recently, Zeising et al. (2024) conducted a study employing high-resolution ground-based and airborne radar measurements alongside satellite remote-sensing observations. Their findings suggest that the hinge zone of 79NG has become channelized and significantly thinner over the last two decades, with the emergence of up to 500 m high subglacial channels since around 2010. The time series of the three Lagrangian in situ basal melt rate profile lines in the vicinity of the grounding line and along the ice flow show rates exceeding 100 m yr^{-1} before 2018. Additionally, they report observations of low melt rates and small ice draft gradients under thick ice, demonstrating high spatial variability of melt rates in the hinge zone.

2.5. Plume Modeling and Its Challenges

Ice shelf water plume models aim to predict the dynamics and physical properties of meltwater beneath the ice shelf, which are influenced by subglacial discharge and the turbulent entrainment of ambient seawater (Beckmann et al., 2018; Begeman et al., 2022; Jenkins, 1991). The conceptual framework of a plume model involves dividing the ice-ocean boundary layer into two dynamical regions (Jenkins et al., 2010): a laminar sublayer positioned directly at the ice-ocean interface and a turbulent mixed layer affected by rotation and stratification (Burchard et al., 2022; Holland & Feltham, 2006; Jungclaus & Backhaus, 1994). In contrast to three-dimensional modeling (Losch, 2008), plume models are not explicitly simulating the ambient ocean. Nevertheless, the computational efficiency of plume models enables finer grid spacing, thereby allowing for the resolution of smaller topographic details, including narrow basal channels. Thus, plume models serve as efficient tools for conducting systematic sensitivity analyses and enhancing our understanding of the role of the different physical processes affecting basal melt.

Several studies have developed plume models and utilized them in a variety of idealized and semi-realistic applications in both Greenland (Gladish et al., 2012) and Antarctica (Holland & Feltham, 2006; P. R. Holland et al., 2009; Lazeroms et al., 2018). However, a challenge in the plume modeling, as highlighted by Gladish et al. (2012), arises when the plume velocity diverges, leading to a reduction in plume thickness and subsequent numerical instability. To mitigate this issue, a minimum water thickness was enforced (Gladish et al., 2012) and enhanced entrainment has been introduced in regions where plume thickness was thin, particularly in the hinge zone (Lambert et al., 2023). However, the imposition of a minimum thickness, especially in the hinge zone, acts as a constant head of water pressure for downstream currents, similar to introducing a continuous subglacial discharge. Consequently, while addressing numerical instability issues, this technique leads to a substantial and constant addition of freshwater to the model, effectively introducing conditions of an efficient drainage system (Dow, 2022). This complicates the understanding of melt rate dynamics, particularly during the dry season (steadier winter conditions with low subglacial discharge), when lower basal melt rates are expected.

3. The General Ice Shelf Water Plume Model (GIPM)

GIPM, the finite-volume, two-dimensional plume model used in this study (Mohammadi-Aragh & Burchard, 2024), is based on time-dependent, vertically integrated prognostic equations. This system of equations represents the buoyant turbulent gravity currents underneath large ice shelves, including basal melting at the ice-

water interface and entrainment of warm, saline water at the bottom of the turbulent plume (Holland & Feltham, 2006; Jenkins, 1991; Jungclaus & Backhaus, 1994).

The governing equations are discretized using a staggered Arakawa C-Grid. Advection is performed through directional-splitting, providing various options for high-order Total Variation Diminishing limiters with minimized numerical diffusion (Klingbeil et al., 2014; Mohammadi-Aragh et al., 2015). The model accommodates the specification of inflow boundaries, outflow boundaries, and closed boundaries where free-slip conditions are enforced. Both flux and water thickness boundaries are possible at inflow boundaries.

To address the general issue of plume water divergence, we implement a drying and flooding algorithm that excludes the local control volume from plume dynamics where the plume thickness falls below a critical value ($D_{\min} = 0.15$ m), while still accounting for its thermodynamic effects. When the plume thickness, influenced by localized melt rate or entrainment, exceeds a critical thickness of $D_{\min} = 0.25$ m, the computational cell is reintroduced into the computational domain.

3.1. Plume Governing Equations

The time-dependent equation describing plume thickness, derived from the conservation of mass under the Boussinesq approximation, is:

$$\frac{\partial h}{\partial t} + \nabla \cdot (\mathbf{u}h) = w_e + \dot{m} \tag{1}$$

here, h represents plume thickness, and $\mathbf{u} = (u, v)$ denotes the depth-averaged horizontal velocity vector. Parameters w_e and $\dot{m}$ indicate the entrainment velocity and melt rate at the ice-water interface, respectively (see below for parameterizations).

The momentum balance within the plume is described by

$$\begin{aligned}
\frac{\partial (hu)}{\partial t} + \nabla \cdot (\mathbf{u}hu) &= -\frac{gh^2}{2\rho_0}\frac{\partial \rho}{\partial x} + g'h\frac{\partial (Z-h)}{\partial x} - C_d|\mathbf{u}|u + hfv \\
\frac{\partial (hv)}{\partial t} + \nabla \cdot (\mathbf{u}hv) &= -\frac{gh^2}{2\rho_0}\frac{\partial \rho}{\partial y} + g'h\frac{\partial (Z-h)}{\partial y} - C_d|\mathbf{u}|v - hfu
\end{aligned} \tag{2}$$

with the basal ice topography Z (representing the vertical position of the ice-ocean interface), the Coriolis parameter f, the drag coefficient C_d, and the buoyancy $g' = g\Delta\rho/\rho_0$, where g denotes the gravitational acceleration, $\Delta\rho = \rho_a - \rho$ represents the density contrast, ρ signifies plume density, ρ_a stands for ambient density and ρ_0 denotes the reference density. The ice-ocean interface depth is updated by considering the ice equivalent of the melt rate. However, it should be noted that our plume model is not coupled with ice dynamics, which limits the accuracy of our approximation of the updated basal ice topography compared to cases where these physical processes are included. The terms on the right-hand side of Equation 2 represent baroclinic forcing (due to lateral density gradients), buoyancy, drag at the ice-water interface, and rotation, respectively. The drag coefficient C_d is computed in accordance with the logarithmic law of the wall:

$$C_d = \max\left(0.0005; \left(\frac{\kappa}{\ln\frac{0.5h + z_0}{z_0}}\right)^2\right) \tag{3}$$

here, $z_0 \approx k_s/30$, where, κ, k_s represent von Karman constant, the characteristic height of the roughness element.

In our experiments, the plume density is approximated by a linear equation of state:

$$\rho = \rho_0\left[1 + \beta_s(S - S_0) - \beta_\theta(\theta - \theta_0)\right] \tag{4}$$

Table 1
Model Parameters

Symbol	Value	Name	Equations
g	9.81 m s^{-2}	Gravitational acceleration	2 and 12
κ	0.4	Von Karman constant	3
S_0	34.5 (g/kg)	Reference salinity	4
θ_0	−2.0°C	Reference temperature	4
β_s	7.86×10^{-4}	Haline contraction coefficient	4
β_θ	3.87×10^{-5} K^{-1}	Thermal expansion coefficient	4
S_i	0 (g/kg)	Salinity of ice	5 and 8
c_i	2,009 J $kg^{-1}K^{-1}$	Specific heat capacity for ice	7
c_w	3,974 J $kg^{-1}K^{-1}$	Specific heat capacity for seawater	7
L_i	3.35×10^5 J kg^{-1}	Latent heat of fusion for ice	7
θ_i	−15.0°C	Ice core temperature	7
λ_1	-5.73×10^{-2}°C $(g/kg)^{-1}$	Seawater freezing point slope	11
λ_2	8.32×10^{-2}°C	Seawater freezing point offset	11
λ_3	7.61×10^{-4}°C m^{-1}	Depth-dependence of freezing point	11
c_l	0.0055	Kochergin entrainment parameter	12
k_s	0.001 m	characteristic height of the roughness element	3

Note. The optimal Kochergin entrainment parameter c_l was obtained by a sensitivity analysis (not shown here).

where absolute salinity S, potential temperature θ, haline contraction coefficient β_s, thermal expansion coefficient β_θ, reference salinity S_0, and reference potential temperature θ_0 are utilized. The empirical parameters employed in the present study are provided in Table 1.

The salinity and potential temperature of the plume are determined by vertically integrating the heat and salt budgets:

$$\frac{\partial(hS)}{\partial t} + \nabla \cdot (\mathbf{u}hS) = w_e S_a + \dot{m} S_b - \gamma^S (S - S_b) \tag{5}$$

$$\frac{\partial(h\theta)}{\partial t} + \nabla \cdot (\mathbf{u}h\theta) = w_e \theta_a + \dot{m} \theta_b - \gamma^T (\theta - \theta_b) \tag{6}$$

where subscripts a denote properties of ambient water and subscripts i denote properties of the ice. θ_b and S_b represent the temperature and salinity at the ice shelf–ocean interface. As defined by Equations 5 and 6, salinity and temperature of the plume rely on lateral advection, entrainment of ambient water, and fluxes across the ice-ocean interface. The terms on the left side represent the advection of salinity and temperature, while the terms on the right side account for the contributions of entrainment, ice shelf melting, and turbulence.

To complete the set of Equations 1–6, parameterizations for the mass, momentum, salt, and heat fluxes through the ice-ocean interface as well as through the bottom of the plume are required. At the ice-ocean interface Z, we employ the 3-equation balance as the most common method to describe melt rate, utilizing the balance of heat and salt flux (Hellmer & Olbers, 1989; D. M. Holland & Jenkins, 1999; Jenkins, 1991):

$$\dot{m} L_i + \dot{m} c_i (\theta_b - \theta_i) = \gamma^T c_w (\theta - \theta_b) \tag{7}$$

$$\dot{m} (S_b - S_i) = \gamma^S (S - S_b) \tag{8}$$

$$\gamma^T = \frac{u_*}{2.12 \ln\left(C_d^{1/2} \mathrm{Re}\right) + 12.5 \mathrm{P_r}^{2/3} - 8.68} \tag{9}$$

$$\gamma^S = \frac{u_*}{2.12\ln\left(C_d^{1/2}\mathrm{Re}\right) + 12.5\mathrm{Sc}^{2/3} - 8.68} \tag{10}$$

with γ as exchange velocity, and Re, $u_*^2 = C_d|\mathbf{u}|^2$ representing Reynolds number, and interfacial friction velocity. Additionally, L_i represents the latent heat of fusion, c_i stands for the specific heat capacity of ice, and c_w denotes the specific heat capacity of seawater (values are provided in Table 1). $\mathrm{Re} = \mathbf{u}h/\nu_0$, where $\nu_0 = 1.95 \times 10^{-6}\mathrm{m}^2\mathrm{s}^{-1}$, Pr = 13.8 represents the molecular Prandtl number, and Sc = 2432 indicates the molecular Schmidt number of seawater.

The temperature at the ice–ocean interface of the plume water, θ_b, is calculated by means of

$$\theta_b = \lambda_1 S_b + \lambda_2 + \lambda_3 Z \tag{11}$$

with the empirical parameters λ_1, λ_2 and λ_3 and a linearization of the liquids relationship, see Table 1. The salinity at the ice shelf–ocean interface, S_b, is estimated using the three equations that describe the balance of heat (Equation 7) and salt (Equation 5) at the ice–ocean interface, along with the liquid condition that must be satisfied there (Equation 11). The thermal driving, θ–θ_b, and the salinity gradient, S–S_b, represent the melt potential of the plume.

To estimate the entrainment velocity, we employ the parameterization proposed by Kochergin (1987), as done in previous studies (Jungclaus & Backhaus, 1994; Payne et al., 2007):

$$w_e = \frac{c_l^2}{\mathrm{S_m}}\sqrt{|\mathbf{u}|^2 + \frac{g'h}{\mathrm{S_m}}} \tag{12}$$

where c_l represents the Kochergin entrainment parameter, $\mathrm{S_m}$ denotes the turbulent Schmidt number (Mellor & Durbin, 1975), and

$$\mathrm{S_m} = \frac{\mathrm{R_i}}{0.725\left(\mathrm{R_i} + 0.186 - \sqrt{\mathrm{R_i}^2 - 0.316\mathrm{R_i} + 0.0346}\right)} \tag{13}$$

with $\mathrm{R_i} = g'h/|\mathbf{u}|^2$ being the gradient Richardson number.

4. Data and Method

4.1. Site Description and Computational Domain

The 79NG has a floating ice tongue measuring approximately 69 km in length and 24 km in width, expanding to around 30 km from its midpoint (Hill et al., 2017, see Figure 1a). It features two calving fronts: one located to the north toward Djimphna Sound, and another to the east distinguished by several ice rises acting as pinning points (Humbert et al., 2023). The floating ice tongue is attached to the fjord's edges and thins from approximately 500 m at the grounding line to 100 m at these anchoring points. Below the floating tongue lies a deep cavity (maximum 900 m), with its deepest section positioned toward the center (Mayer et al., 2000). A bottom-intensified flow transports warm, saline water into the cavity over an underwater sill near the calving front (Schaffer et al., 2020). Notably, no warm inflow along Djimphna Sound toward the northeastern calving front of the ice tongue has been observed (Lindeman et al., 2020; Schaffer et al., 2020), presumably due to a sill at the fjord mouth inhibiting such movement (Wilson & Straneo, 2015).

The domain of interest, highlighted in cyan in Figures 1a and 2a, is discretized using a structured, equidistant grid with a spacing of 150 m. We extend the computational domain beyond both termini of the ice tongue. Further downstream of the eastern calving front, an outflow boundary condition with zero gradients (zero scalar flux) is applied at a distance equal to half the length of the ice shelf.

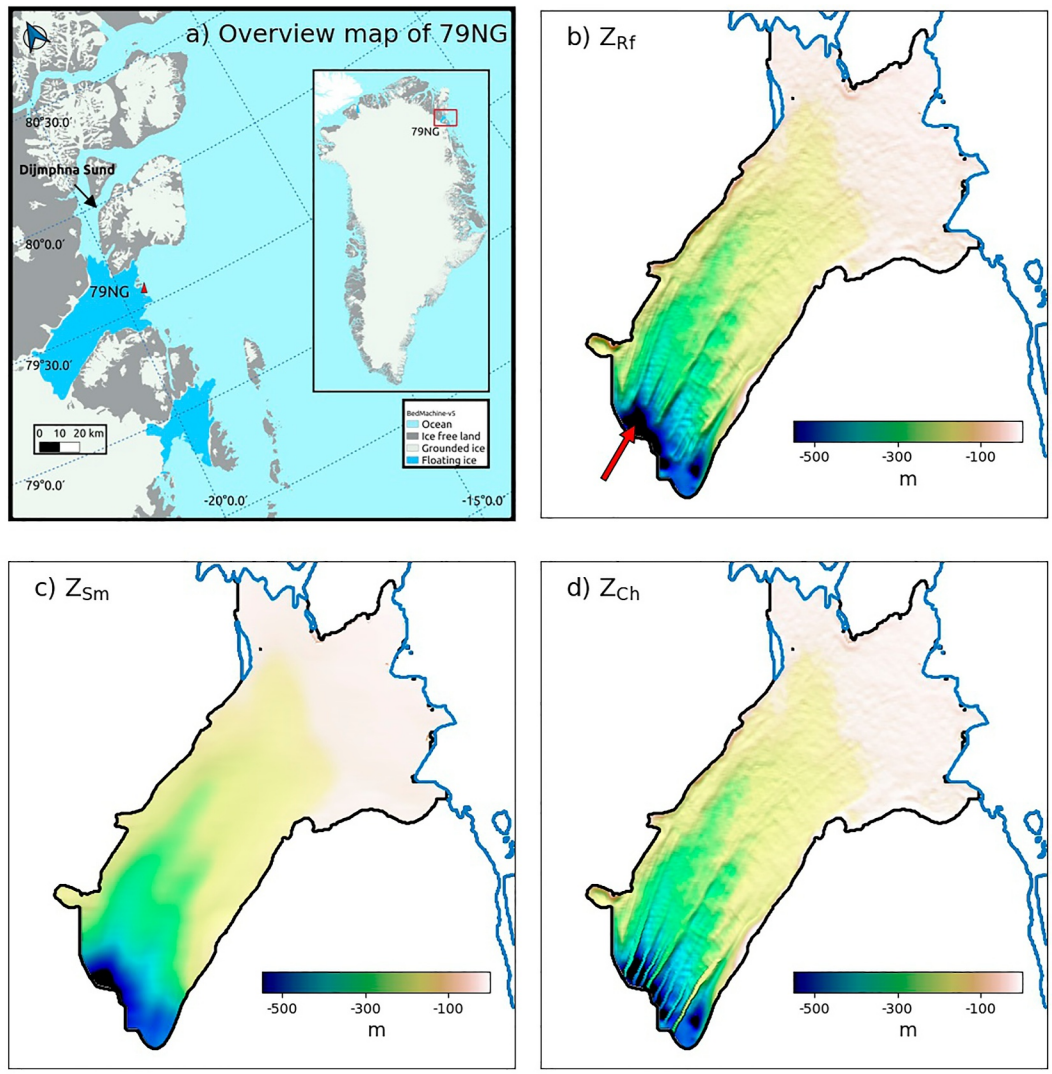

Figure 1. (a) Overview map of the 79NG ice shelf, with ice shelves depicted in cyan. The red triangle marks the locations of the three CTD profiles collected in front of the main calving front. This map was generated using BedMachine Greenland version 5 data set (Morlighem et al., 2017a). Comparison of ice base topographies used in the simulations: (b) Z_{Rf}, (c) Z_{Sm}, and (d) Z_{Ch}.

4.2. Ice Thickness Data Set, Filtered, and Channelized Ice Base Topographies

Ice thickness data set: We use BedMachine Greenland version 5 (Morlighem et al., 2017a). The ice base topography is obtained by determining the difference between the ice surface elevation and ice thickness. This data set is produced using data collected from 1993 to 2016, with a nominal reference date of 2007. It provides gridded ice surface elevation and ice thickness, with a horizontal grid spacing of 150 m. Table 2 summarizes the labels and characteristics of the ice base topographies mentioned in our sensitivity analyses.

Filtered ice base topographies: To generate ice-base topographies with varying degrees of smoothness, we applied spatial averaging filters with widths that were successively increased by 0.6 km, starting at 0.75 km (reference ice base topography, Z_{Rf} (Figure 1b)) and ending at 3.75 km (smooth topography, Z_{Sm} (Figure 1c)).

Channelized ice base topography: The ice base topography Z_{Ch} containing channels (Figure 1d) is configured by carving a network of large and small basal channels, that is extreme roughness of the base, into the hinge zone of Z_{Rf}. The length, width, orientation and arrangement of these channels (Figure 2a) are inspired by a realistic ice thickness data set that covers only the hinge zone of 79NG, representing the year 2021 (Zeising et al., 2024). The

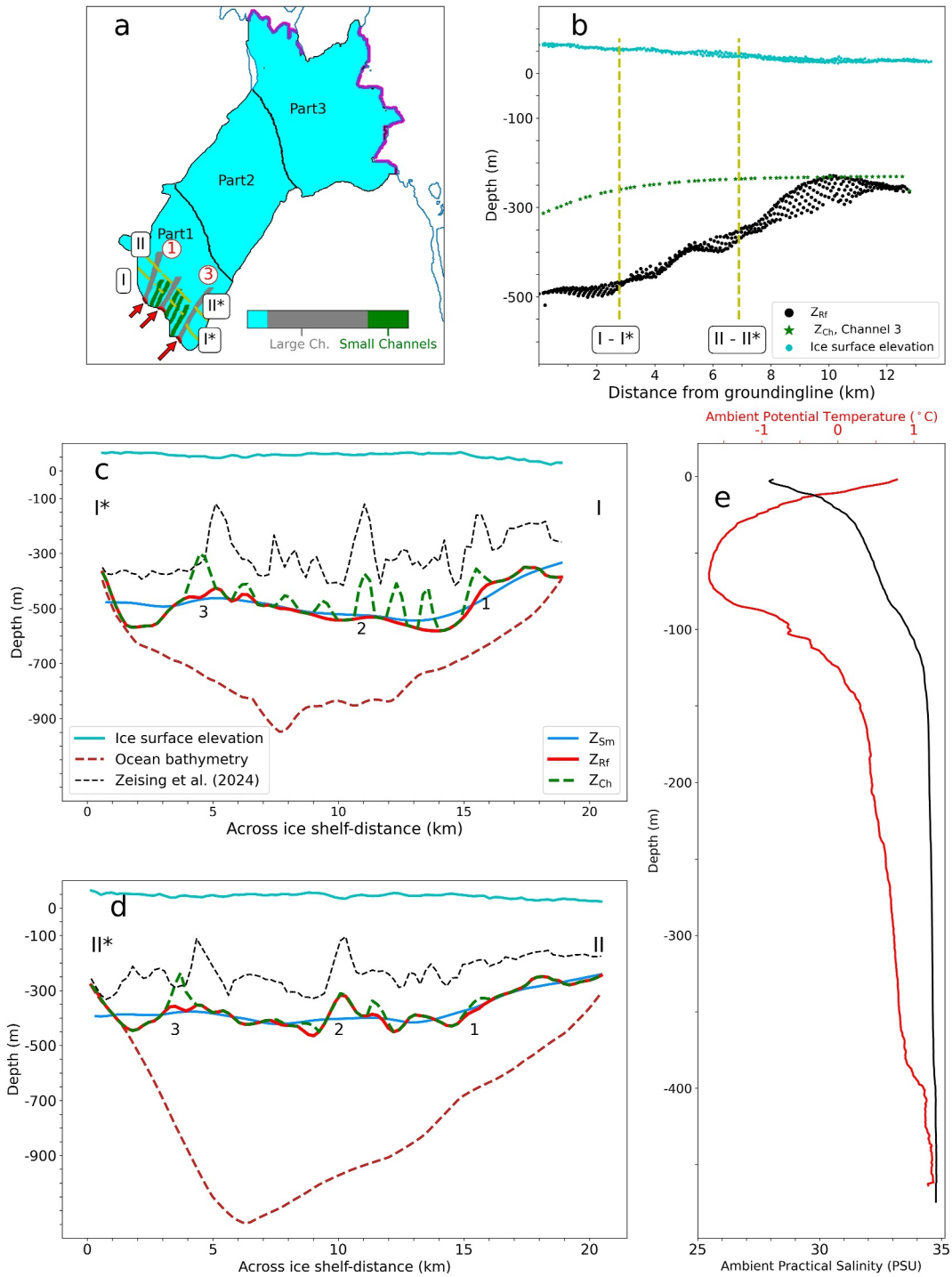

Figure 2. Oceanographic setting and geometrical characteristics of basal channels: (a) Arrangement of basal channels which are added to Z_{Rf}. The numbers indicate the naming pattern of the channels from the northern side to the southern side of the ice shelf. The yellow lines crossing the ice shelves are cross sections shown in panels (c) and (d). The location of channelized discharge in front of the three large basal channels is indicated by cells in red and red arrows. The channelized discharge is located in these three locations based on the work of Narkevic et al. (2023) and Z. Wang et al. (2020). The magenta color at the calving front indicates the areas where plume water exits the ice shelf cavity and enters the ocean. The ice shelf is divided into three regions for a comparison of the spatial mean melt rate. (b) The along channels sections of Z_{Ch} and Z_{Sm} along the large channel, number 3 in panel (a). (c) The Cross-Section of ice base topographies along I-I* as shown in panel (a). (d) The Cross-Section of ice base topographies along II-II* as shown in panel (a). (e) Temperature (red) and salinity (black) profiles, averaged over three CTD casts (Kanzow et al., 2017) taken in front of the main (eastern) calving front of the floating ice tongue (see Figure 1).

Table 2
Spatial Filters, Ice Base Topographies and Experiments

Spatial filters						
Name of Filter	f_1	N/A	N/A	N/A	N/A	f_2
Size (km)	0.75	1.35	1.95	2.55	3.15	3.75
LVT_{avg}	0.0073	0.0073	0.0041	0.0037	0.00353	0.0033
Ice base topographies						
Label		Z_{Rf}		Z_{Sm}	Z_{Ch}	
Filter		f_1		f_2	f_1	
Channels		N/A		N/A	Yes	
Experiments						
Label		EZ_{Rf}		EZ_{Sm}	EZ_{Ch}	
Ice Base Topographies		Z_{Rf}		Z_{Sm}	Z_{Ch}	

Note. LVT_{avg} is the spatial mean of the Local Variation of Topography (LVT) defined in Section 4.5. Subglacial discharge presence/absence is addressed through impact studies (Section 5.2.3), eliminating the need for additional experiment labels. The experiment with reference topography, Z_{Rf}, and without subglacial discharge is referred to as the *Reference* experiment. Simulations with warm discharge at 1.5°C and sensitivity to cold discharge (0°C) are also discussed in Section 5.2.3.

channels are positioned in the hinge zone, aligned with the preexisting channels in the ice thickness data set downstream of the hinge zone crossing the grounding line, since these channels exist in the hinge zone in reality (Zeising et al., 2024) but are not represented in the data set (see Figure 1b). We classify the channels as large if they are wide and long, and as small if they are narrow and short. The width of all large channels increases from several hundred meters to 1 km along the direction of ice flow, while the width of the small channels remains nearly constant at less than 1 km.

To configure the large channels, we describe their height as an exponential function, $H(x)$, decreasing with distance from the grounding line, x,

$$H(x) = H_0 \exp(-b \cdot x) + C, \tag{14}$$

with $H_0 = 200$ m, and with $b = 0.14 \times 10^{-3}$ to $b = 0.66 \times 10^{-3} m^{-1}$, representing an e-folding length of maximum 7.14 km. The small channels are given by Equation 14 with $H_0 = 100$ m and $b = 0.36 \times 10^{-3}$ m^{-1}. The parameters b and C for both large and small channels are adjusted to ensure a smooth transition at their termini, avoiding any discontinuities with the ice shelf.

The section of large channel number 3 of Z_{Ch} is shown in Figure 2b. Figures 2c and 2d show the cross-sections of all ice shelves used in this study (see Table 2). Both compare the cross-sections from the hinge zone of Z_{Ch} and the ice base topography produced by Zeising et al. (2024). Despite the large ice thinning suggested by Zeising et al. (2024)'s data set at the hinge zone, the shape and arrangement of the channels, as well as the rate of reduction in their height between the two cross-sections, are similar, demonstrating the success of channels in capturing the realistic geometry of channelized ice shelves.

4.3. Forcing

Oceanic forcing: We use Conductivity-Temperature-Depth (CTD) profiles taken from R/V Polarstern cruise PS100 in summer 2016 (Kanzow et al., 2017) right in the pathway where warm Atlantic Intermediate Water flows toward the subglacial cavity (Schaffer et al., 2020). To enforce temperature and salinity of the ambient water at the lower boundary of the plume water, we use the average of three CTD profiles taken in front of the main calving front (see Figures 1a and 2e). The model is standalone, with ocean forcing calculated based on the assumption of stagnant ambient water masses. The ambient water conditions (S_a and T_a) are taken from the CTD profile at the depth of the ocean-plume interface.

Subglacial discharge: We conducted simulations for two cases: one where the subglacial discharge with potential temperature of 1.5°C is distributed uniformly along the grounding line, referred to as grounding line discharge, and another where it is introduced through three wide channels located in front of the three large basal channels, indicated by red cells and shown by red arrows in Figure 2a. We performed a series of experiments testing the sensitivity of the basal melt rates to the subglacial discharge, ranging from no discharge (dry season) to a maximum of 242.19 km^3 yr^{-1} during a 3-month melting season. The actual temperature of the subglacial discharge is unknown, but it can increase with the travel distance of water beneath the glacier due to dissipation and turbulent motion (Beyer et al., 2018). The 79NG acquires water from far upstream along the Northeast Greenland Ice Stream. Zeising et al. (2024) analyzed the skin temperature, which was partially around 1.35°C, supporting our assumption of a potential temperature maximum of 1.5°C of subglacial discharge. In a series of simulations, we also repeated the grounding line subglacial discharge distribution experiments assuming a temperature of 0°C.

4.4. Modeling Strategy

The experiments start with an initial condition of stagnant plume water and a uniform initial plume thickness of 5 m. This modeling approach accounts for the ocean's effect while ignoring the effects of ocean circulation. The

Kochergin number, serving as a direct control for the heat influx to the plume water, is set so that the spatial mean melt rate matches the order of the diagnosed spatial mean melt rate by Wilson et al. (2017). The simulations run until a quasi-steady state in the spatially mean melt rate is reached, that is, when the value becomes nearly constant, as confirmed by visual inspection, for all experiments. Experiments were categorized based on the ice base topography used. Table 2 presents the degree of smoothness using LVT, the spatial filter size, and whether channels are introduced to the hinge zone. Note that we resolve roughness features larger than the model's grid spacing, while the effects of roughness smaller than the grid spacing are introduced into the model through the melt rate parameterization and the diagnosed drag coefficient. The presence or absence of subglacial discharge was examined through sensitivity analyses (Section 5.2.3), eliminating the need for additional experiment labels. Simulations were performed with warm subglacial discharge at 1.5°C, and the sensitivity to cold subglacial discharge (0°C) is discussed in Section 5.2.3. We note that not all possible combinations of these parameters were simulated in this analysis but values were chosen that best reflects differing conditions.

4.5. Analyses and Metrics

4.5.1. Local Variation of Topography

We measure the roughness of ice base topographies, defined as the Local Variation of Topography (LVT)

$$\mathrm{LVT}_{j,i} = \frac{1}{N_{j,i}} \sum_{n=-1}^{1} \sum_{m=-1}^{1} \left| \frac{Z(j,i) - Z(j+n, i+m)}{Z(j,i) + Z(j+n, i+m)} \right|, \tag{15}$$

where $N_{j,i}$, j, i are the number of pairs of adjacent computational cells with the central grid point, and indices of cells in both directions of the computational coordinate, respectively. $N_{j,i}$ is maximum 8. LVT can be interpreted as the slope factor (Sikirić et al., 2009) in a one-dimensional domain. For all topographies, the average LVT values are given in Table 2.

4.5.2. Passive Tracer Investigation

In order to track the pathways of warm ambient water that is entrained into the plume as it flows along the ice shelf toward the calving front, we analyzed the distribution of a passive tracer. The passive tracer experiments are conducted with grounding line discharge rate of 4.8 mSv. The source of the passive tracer is defined as the region where the ambient water temperature exceeds 0.9°C, a threshold arbitrarily chosen to differentiate between warm and cold water, with the specified warm water being entrained up to approximately 10 km from the grounding line, below the ice tongue.

Passive tracer enters the computational domain via entrainment where the ambient water exceeds the temperature of 0.9°C. Naturally the tracer flux varies with entrainment volume which depends on the ice base topography.

4.5.3. Annual Melt Rate

To calculate the annual melt rate, we performed two separate simulations based on a simplifying assumption: one for the dry season with no subglacial discharge, and another for the melting season with a constant, grounding line discharge. The melting season was defined as a 3-month period with a constant discharge rate, while the dry season was assumed to last 9 months without any subglacial discharge. The annual melt rate was then calculated by averaging the melt rates from these two simulations over 1 year. It is important to note that each season was simulated independently, assuming constant subglacial discharge. We thus assumed that ice conditions remained consistent throughout each period and that any melting ice was replenished by the ice stream.

5. Results

5.1. Basal Melt Rate of the *Reference* Experiment

The melt rate distribution of our experiment with reference topography, $\mathrm{EZ}_{\mathrm{Rf}}$, without subglacial discharge (Figure 3a) shows low to moderate melt rates with a spatial mean of 6.65 m yr^{-1}. The melt rate distribution in the hinge zone is characterized by low melt rates, which transition to moderate melt rates in the form of linear

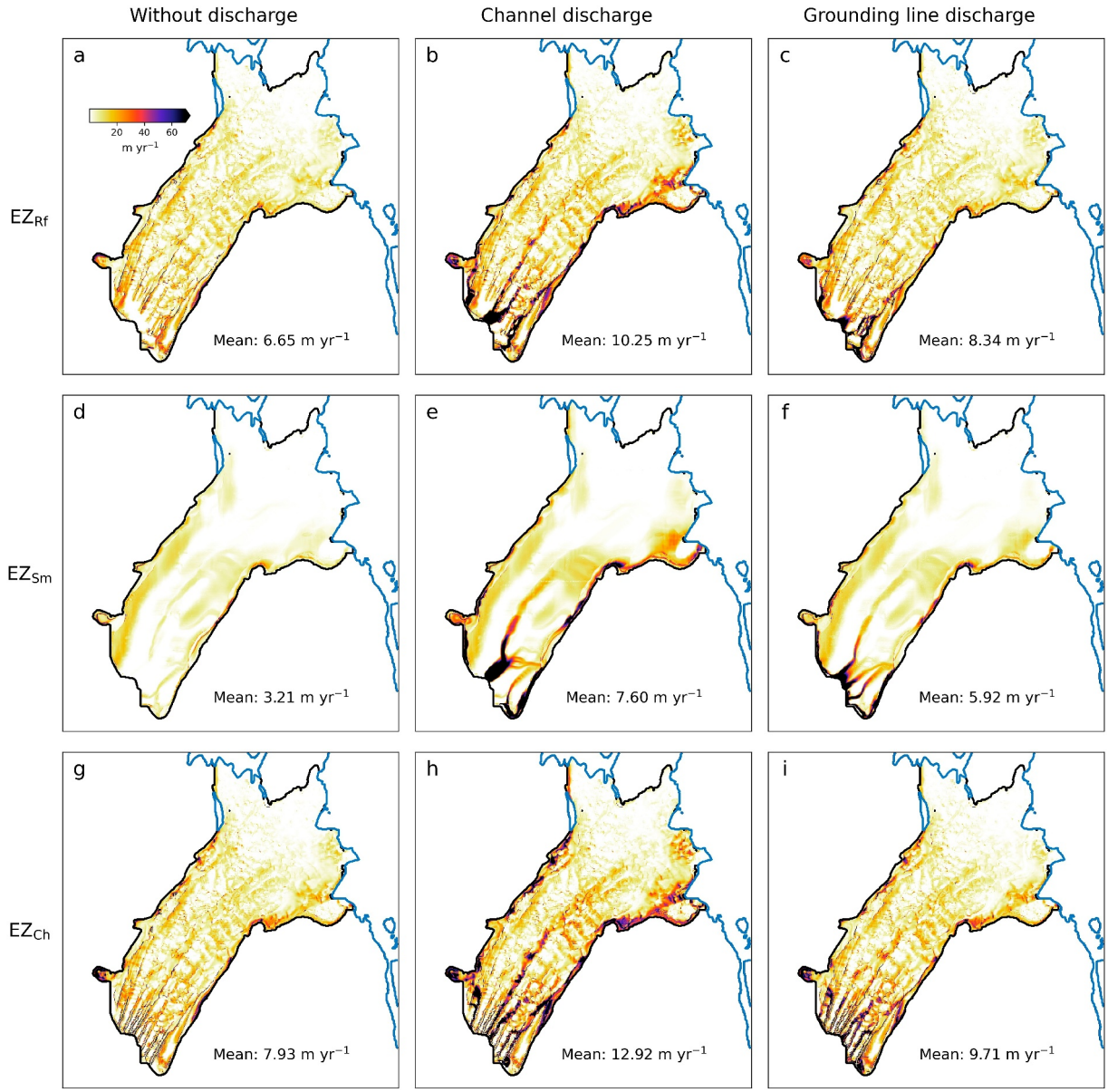

Figure 3. Comparison of snapshots of the basal melt rate for three scenarios: without discharge (first column), channelized discharge (second column), and grounding line discharge (third column). The experiments were conducted using Z_{Rf} (first row), Z_{Sm} (second row), Z_{Ch} (third row). Note that the melt rate maps in this figure do not represent the annual melt rate. Additionally, the discharge rate used is 4.8 mSv.

channels a few kilometers from the grounding line. As the distance to the hinge zone increases, melt rate intensity gradually diminishes, and the occurrence of scattered features increases over linear features.

The ratio of the annual spatial mean melt rate in the hinge zone (Part 1, Figure 2a) to that at the calving front (Part 3) ranges from 4 to 5, indicating a significant decrease in melt rate from the grounding line toward the calving front (shown in Section 5.2.3).

5.2. Sensitivity Studies

5.2.1. Impact of Basal Roughness

The investigation of the impact of basal roughness on the melt rate is based on configurations without subglacial discharge, meaning the melt rates we compare are not annual averages (averaged over dry season). The

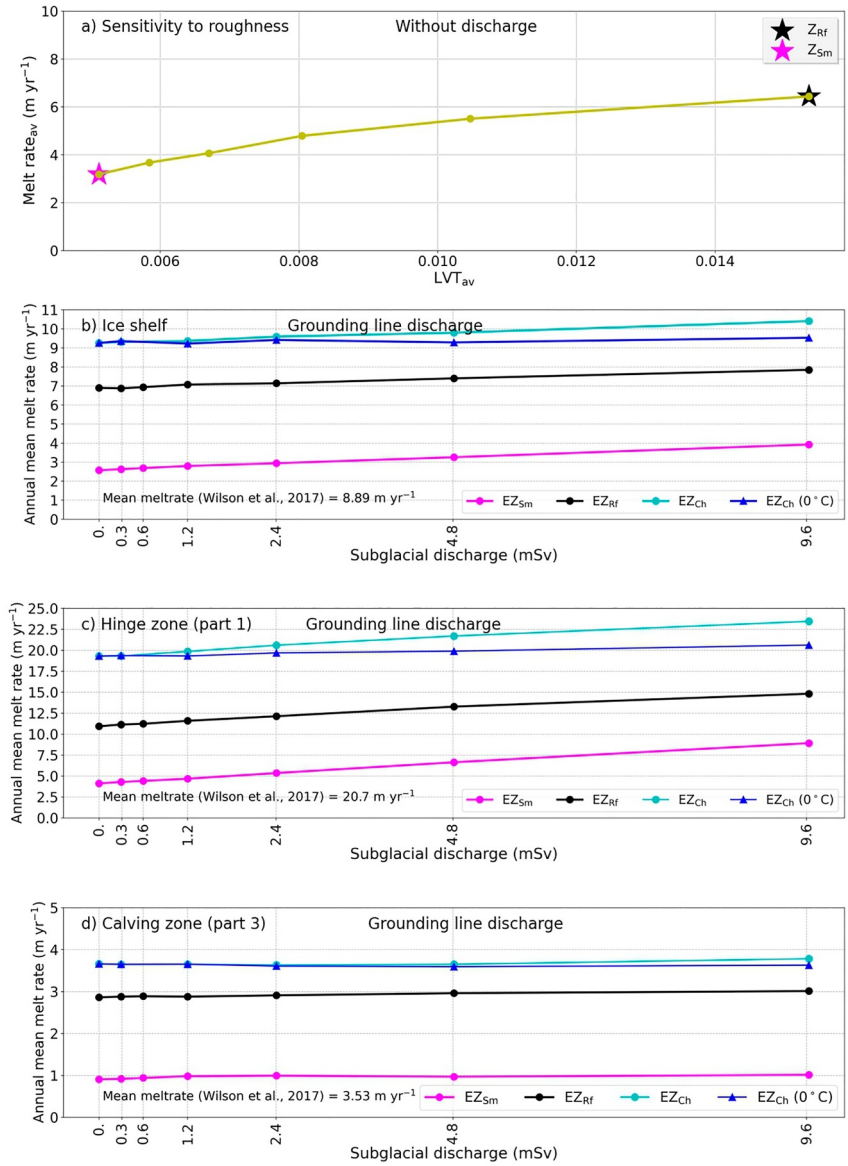

Figure 4. Analysis of basal melt rates under various subglacial discharge conditions and ice base roughness: (a) Impact of ice base roughness on the spatially averaged melt rate, without considering subglacial discharge. The area-averaged basal melt rate of the floating ice tongue is shown for simulations with different ice base topographies and varying subglacial discharges, for: (b) the entire ice shelf, (c) the hinge zone, and (d) the calving zone. These partitions are illustrated in Figure 2a.

comparison of the two experiments with the reference (Z_{Rf}) and the smooth (Z_{Sm}) topographies exhibit the greatest difference in basal melt rates. The mean spatial melt rate of EZ_{Sm} (Figure 3d) is reduced by 3.44 m yr^{-1} (or 52%) compared to EZ_{Rf} with a rough ice base. In EZ_{Rf}, moderate melt rates are more scattered across the domain, whereas EZ_{Sm} shows moderate melt rates only at the margins of the ice shelf. Near the grounding line, the basal melt rate in both experiments does not exhibit high or extreme values. Another analysis of basal roughness, showing the sensitivity of the spatial mean melt rate to domain-average roughness, is presented in Figure 4a. It reveals that increasing the domain-average roughness of ice base topographies monotonically increases the spatial mean melt rate.

5.2.2. Impact of Basal Channels in the Hinge Zone

Similar to the previous analysis, we investigate the impact of basal channels in the hinge zone on the melt rate without subglacial discharge. We compare the basal melt rates from EZ_{Rf} and EZ_{Ch}, as shown in Figures 3a and 3g. EZ_{Rf} is characterized by rough ice base topography, whereas EZ_{Ch} in addition incorporates basal channels. EZ_{Ch} exhibit generally moderate melt rates across the entire domain. However, in a region several kilometers from the grounding line, EZ_{Rf} shows low to moderate melt rates, while EZ_{Ch} displays moderate to high melt rates, underscoring the significance of channels in the hinge zone. The mean spatial melt rate of EZ_{Ch} is 1.28 m yr^{-1} (or 19%) higher than EZ_{Rf}, illustrating the localized effect of basal channels in the absence of subglacial discharge. It should be emphasized that the plume model we are applying here is hydrostatic. This entails that the stress at the ice-ocean interface and therefore the melt rate becomes inaccurate if the slope $\partial(Z-h)/\partial x$ or $\partial(Z-h)/\partial y$ in Equation 2 is too steep. Note that for a vertical interface as in tidewater glaciers the slope would become unbounded. However, since the steepest slope angle in our study is only about 17° and affects only a very small portion of the ice shelf, our approximation of melt rates remains valid, with minimal uncertainty in the estimates.

5.2.3. Impact of Subglacial Discharge

We investigate the influence of subglacial discharge distribution—either through the grounding line or channelized discharge—on the basal melt rate pattern, as well as the impact of discharge intensity on the annual spatial mean melt rate. The comparison of basal melt rate patterns is based on experiments with subglacial discharge of 4.8 mSv.

Experiment EZ_{Rf} (Figure 3a) exhibits low to moderate melt rates at the grounding line in the absence of subglacial discharge. However, when either channelized (Figure 3b) or grounding line (Figure 3c) discharge is introduced, a localized high to extreme melt rate is generated in the hinge zone. The mean melt rate is 3.60 m yr^{-1} (or 54%) higher in the experiment with channelized discharge than without subglacial discharge. In the experiment with an input flux through the grounding line, the melt rate is more evenly distributed and increased by only 1.69 m yr^{-1} (or 25%) compared to the experiment without subglacial discharge.

Experiment EZ_{Sm} (Figure 3d) exhibits low melt rate at the grounding line in the absence of subglacial discharge. However, when either channelized (Figure 3e) or grounding line (Figure 3f) discharge is introduced, a localized high to extreme melt rate is simulated in the hinge zone. Similar to EZ_{Rf}, the melt rate intensity is higher in the experiment with channelized discharge (4.39 m yr^{-1} or 137%) but is more evenly distributed when the input flux occurs through the grounding line (2.71 m yr^{-1} or 84%). Different from EZ_{Rf}, for both types of discharge, the melt rate intensifies in three broad bands: two along the northern and southern margin zones, and one along the central band of the ice shelf.

Experiment EZ_{Ch}, without subglacial discharge, shows a high melt rate with linear features near the grounding line (see Figure 3g) and low to moderate melt rate in the rest of the domain. Introducing subglacial discharge results in extreme melt rates within the channels in the hinge zone (Figures 3h, 3i, 6c, and 6d). This is also evident in Figures 6c and 6d. However, in the experiment with channelized subglacial discharge, the melt rate inside the channels remains elevated further downstream along the ice shelf compared to the grounding line discharge experiment (Figures 3h and 3i). With a grounding line discharge, the melt rate is more evenly spread near the grounding line. The mean spatial melt rate of EZ_{Ch} with a channelized discharge is 4.99 m yr^{-1} (or 62%) higher than the experiment without subglacial discharge and the grounding line discharge is 1.78 m yr^{-1} (or 22%) higher.

The second objective of this sensitivity study is to examine how the annual spatial mean melt rate varies with increased subglacial discharge. Our results, shown in Figure 4b, indicate that a gradual increase in subglacial discharge only slightly enhances the annual mean melt rate across all experiments, with an increase of approximately 1 m yr^{-1} across annual flux range from 0.3 to 9.6 mSv. A closer inspection reveals however that the annual spatial mean melt rate near the grounding line, averaged over Part 1 in Figure 2a, is about twice as high as the annual mean spatial melt rate for the entire ice shelf. The greatest variation in annual mean melt rate due to increase of discharge is noted in the hinge zone (Part 1), where it reaches 4 m yr^{-1} (Figure 4c), while the melt rate in the calving zone (Part 3) remains almost invariant (Figure 4d). However, the series of simulations with cold discharge shows no sensitivity of the spatial mean melt rate to discharge, neither in the regions near the grounding line and the calving front nor over the domain as a whole.

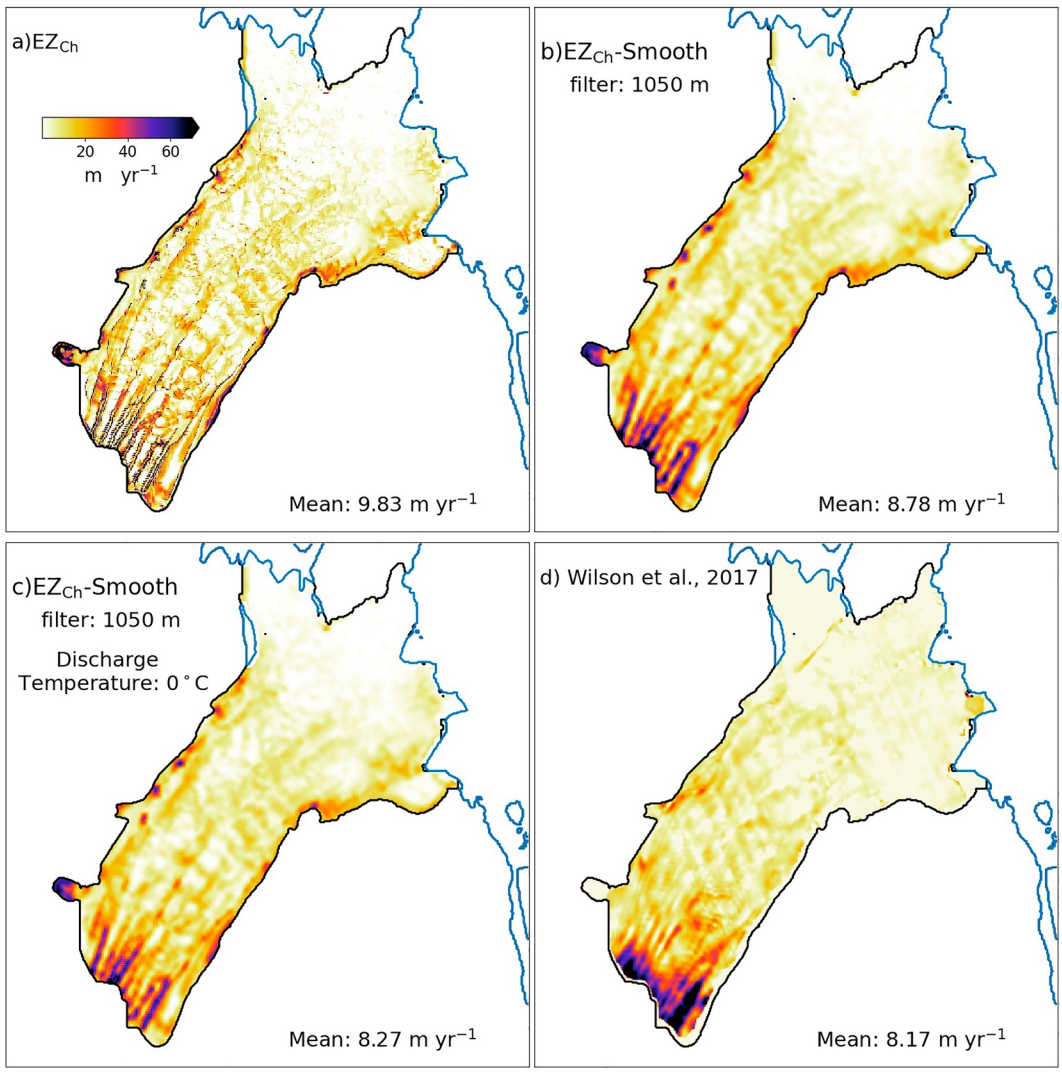

Figure 5. Comparison of the annual basal melt rates for the experiments using (a) EZ_{Ch}, (b) estimated melt rate EZ_{Ch}, smoothed over a spatial scale of 1,050 m, (c) estimated melt rate EZ_{Ch} performed with cold discharge, smoothed over a spatial scale of 1,050 m, and (d) the results from Wilson et al. (2017). Note that the melt rate map represents the annual mean melt rate, accounting for a 3-month melting season and 9 months with grounding line discharge of 4.8 mSv.

6. Discussion

6.1. Comparison With Observation-Based Estimates

We refined the plume model regarding annual spatial mean melt rate by adjusting the Kochergin entrainment parameter c_l. This parameter tunes the heat transfer from ambient water to plume water through the entrainment process Equation 12. We set c_l to 0.055, resulting in an annual spatial mean melt rate for EZ_{Ch} without subglacial discharge that matches the spatial mean melt rate estimated by Wilson et al. (2017).

A spatial comparison of two basal melt rate patterns is meaningful only when performed at the effective resolution (Ebert, 2009), rather than at their nominal grid resolutions (see Mohammadi-Aragh et al., 2020). This is due to numerical diffusion, subgrid parameterizations, and filtering inherent in the models used for both prognostic and diagnostic methods. The effective resolution is defined as the smallest spatial scale at which a high-resolution target product can capture the spatial scale from a coarser and smoother reference product.

The annual melt rate of EZ_{Ch} (Figure 5a) exhibits sharper spatial features than the estimated basal melt rate from Wilson et al. (2017), shown in Figure 5d. The greater sharpness provides a higher level of useful information. It

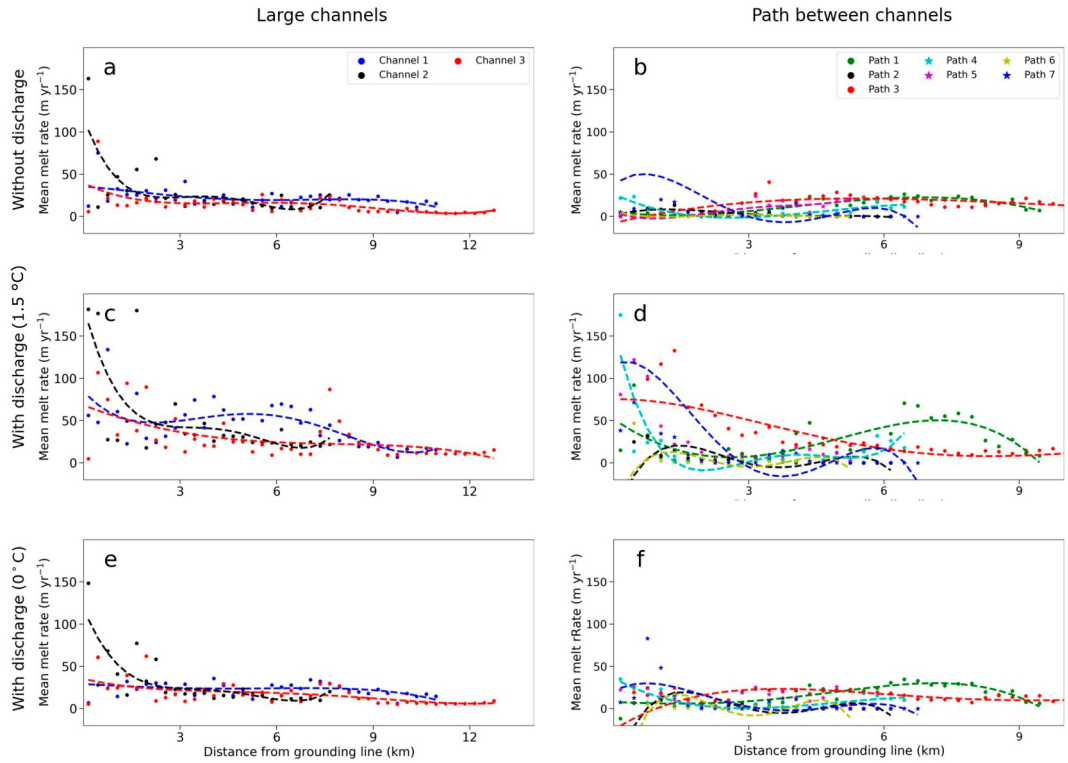

Figure 6. Comparison of melt rates in glacial channels and paths between channels for different scenarios. The first column shows the melt rate within large subglacial channels under three conditions: without subglacial discharge (upper), with grounding line discharge (middle), and with the grounding line cold discharge (lower). The second column presents the melt rates for paths between the channels under the same conditions as the first column.

arises from resolving small-scale features in rough ice base topographies in our study, which significantly impacts the spatial mean melt rate. To align all melt rates to a common spatial scale, we applied a moving average filter with a 7-cell window that reduced the resolution discrepancies and allowed us to focus on broad patterns. This process ensures a meaningful visual comparison by maintaining consistency in spatial scale. The results of EZ_{Ch} for the cases with grounding line discharges of 1.5°C (Figure 5b) and 0°C (Figure 5c), respectively, both smoothed with a spatial filter of 1,050 m, exhibit a good agreement with the basal melt rate map of Wilson et al. (2017). The basal melt rates estimated by G. Wang et al. (2024) and Millan et al. (2023) are provided on a higher resolution grid of 150 m (Figure A1) and show finer structures that compare well with our annual melt rate of experiment EZ_{Ch}, particularly the melt rate map by G. Wang et al. (2024).

Our results demonstrate that melt rates in the hinge zone along the large basal channels generally decrease rapidly from the grounding line toward the calving front, independent on the subglacial discharge (Figures 6a, 6c, and 6e). This is in agreement with the findings of Zeising et al. (2024). The high melt rate at the grounding line reaches a maximum of 100 m yr^{-1} in the absence of subglacial discharge or with a cold discharge. It also increases further to an extreme rate of approximately 150 m yr^{-1} when warm subglacial discharge with a potential temperature of 1.5°C is present. This matches the observations of Zeising et al. (2024) who found melt rates of up to 150 m yr^{-1} in summer near the grounding line. In the paths between the channels, when subglacial discharge is present, melt rates consistently decrease with distance from the grounding line (Figure 6d).

6.2. Plume Water Dynamics

In this section, we compare and discuss the key characteristics of plume water dynamics across the three experiments. These characteristics are essential for understanding the behavior of the plume as it flows beneath the ice shelf. Plume speed determines its motion, while plume thickness and distribution explain both its vertical and horizontal extent. Entrainment describes the mixing of the plume with ambient waters. The entrainment flux is a function of velocity and plume thickness, and a function of the parametrized ambient water properties S_a and T_a.

Additionally, we explore the drag coefficient to quantify the resistance experienced by the plume as it interacts with the rough under-ice surface. The drag coefficient plays an important role in determining how frictional forces slow down the plume, impacting its flow velocity. While the thermal exchange coefficient theoretically has the potential to cause spatial variability in melt rates, our analysis (not shown) suggests that it is of secondary importance compared to thermal driving and requires further exploration in a dedicated boundary layer study. Although the melt rate is sensitive to basal channel height and slope—since they influence plume speed through buoyancy changes, which in turn affect entrainment, plume thickness, and the diagnosed drag coefficient—our results (not shown here) emphasize the greater importance of thermal driving from plume water drainage into the basal channels.

In plume models, the heat for melting at a specific location comes from two primary sources: direct transfer from the ambient water through localized entrainment, and the advection of warm plume water. In addition, the 79NG is located in eastern Greenland (Malyarenko et al., 2020), where melting ablation dominates over dissolving ablation. A visual comparison of our results (not shown) reveals greater spatial variability in the thermal driving field than in the salinity gradient field, highlighting its dominant role in driving the spatial heterogeneity of melt rates. This suggest that a layer of meltwater forms next to the interface, with the phase change driven by heat transfer. This shows how thermal driving, defined as $\theta - \theta_b$, propagates throughout the domain, providing heat for melting across the ice shelf. Thermal driving is not a conservative quantity as it captures the temperature gradient driving heat transfer at the ice-ocean interface. As such, it remains a useful indicator for comparing regions of higher or lower melt intensity in our study. The tracer flows through ice shelf thickness, such as margins and basal channels, as shown by the ice drafts in Figure 1. The area of the tracer source, the region between the red line and the grounding line in Figures 7a–7c, is nearly the same across all experiments. However, the coverage area of tracers beneath the ice shelf is largest in the channelized experiment (EZ_{Ch}), approximately 1.75 times greater compared to EZ_{Sm} and 1.26 times greater compared to EZ_{Rf}. In comparing the tracer spatial distribution with the basal melt rate pattern, presented in the last column of Figure 3, we found similar ratios of spatial mean melt rate in EZ_{Ch} to EZ_{Sm} and EZ_{Rf}, which are 1.64 and 1.16, respectively. Visual inspection comparing the tracer coverage area with the melt rate also reveals a strong correlation.

The tracer studies show the drainage of plume water into shallower regions and basal channels (Figures 7a–7c) where the plume becomes thicker (Figures 7d–7f). In the channels, the plume thickness ranges from about 5 to 10 m, while in the ice shelf margins it can reach several tens of meters. In contrast, the plume thickness for all experiments in other parts of the domain is <1 m. The channelized and reference ice base topographies facilitate the distribution of plume water across the domain, guiding it through the channels and shallower regions. This results in a wide distribution of thermal forcing across the domain through the channels, and an increase in the potential for melting, as shown in Figures 7g–7i.

The melting power of the plume decreases with the travel distance from the grounding line. This is due to the increasing distance from the source of warm entrained water and the depletion of its thermal energy. Additionally, the plume thickness of $5 \sim 10$ m in our simulations is insufficient to fill the channels. Consequently, there is no possibility for the plume water to exit the channels midway; rather, it drains along the entire length of the channels. The width of the larger channels increases along their length, reaching a maximum of 1.5 km at their termini. This width is smaller than the Rossby radius of deformation R_d, which is estimated to be 2.16 km:

$$R_d = \frac{\left(g_c' h_c\right)^{1/2}}{|f|}, \tag{16}$$

as the length scale at which Earth's rotation becomes significant. Here, $g_c' = g\frac{\Delta\rho}{\rho_0}$ and h_c represent the reduced gravity and the plume thickness inside the channels, respectively. Assuming typical values of $\rho_0 = 1025$ kg m^{-3}, $\Delta\rho = 2$ kg m^{-3}, $h_c = 5.0$ m, and a Coriolis parameter of 1.4301×10^{-4} s^{-1}. This suggests that the plume flow does not circulate within the channels to laterally mix thermal energy along their length. It is important to note that the width of the channels we studied here is more similar to the dimensions described by K. E. Alley et al. (2022), which indicate that basal channels across Antarctica and Greenland typically range from 1 to 3 km in width. This contrasts with the idealized basal channels studied by Gladish et al. (2012) and Millgate et al. (2013) which have widths ranging from 2.5 to 20 km, with a single larger channel having the potential to span the entire width of the 79NG ice shelf.

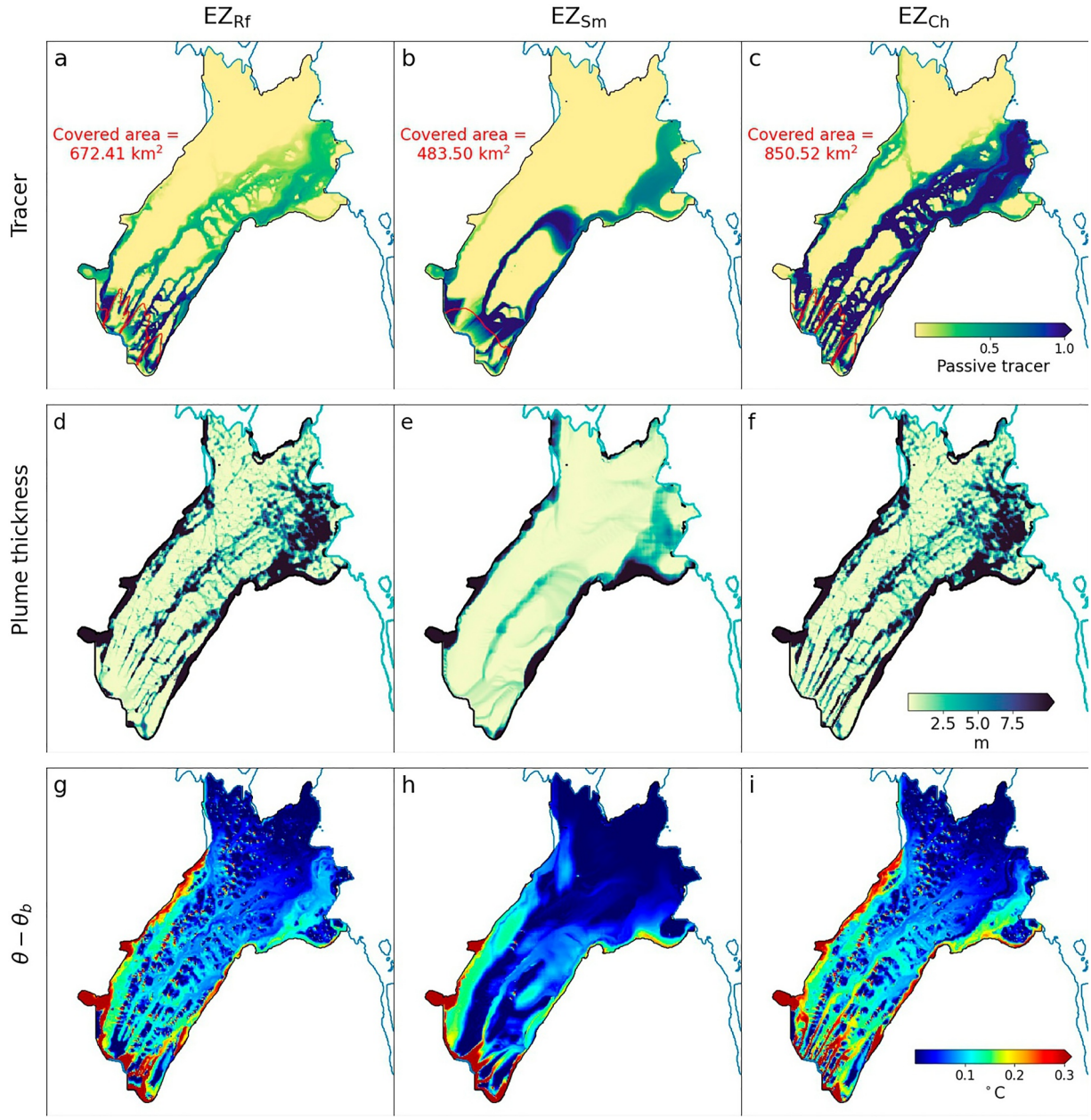

Figure 7. Comparison of different plume characteristics and passive tracer concentration. The first row depicts the trajectories of a passive tracer (a–c), the second row displays plume thickness (d–f), and the third row shows thermal driving for three experiments with a grounding line discharge of 4.8 mSv (g–i). Each experiment utilizes different ice base topographies: Z_{Rf} (first column), Z_{Sm} (second column), and Z_{Ch} (third column). The area between the red line and the grounding line in panels (a–c) is the source area of the tracer release.

The drag coefficient in our simulations depends on the plume thickness (see Equation 3), with thicker plumes having a smaller drag coefficient. Comparing Figures 8a–8c, we see that for all three experiments, the drag coefficient is lower inside the channels and shallower regions at the margins of the ice shelf, providing less potential for resistance against plume movement compared to other regions. Consistent with the lower drag coefficients, plume speeds inside the channels and at the ice shelf margins are up to 5 times higher than in other regions (Figures 8d–8f). The final comparison in the last row of Figure 8 shows that entrainment is more widely distributed across the domain in the EZ_{Ch} and EZ_{Rf} scenarios compared to EZ_{Sm}, indicating greater mixing with ambient water. The shallower regions and channels exhibit higher rates. Therefore, the basal channels within the

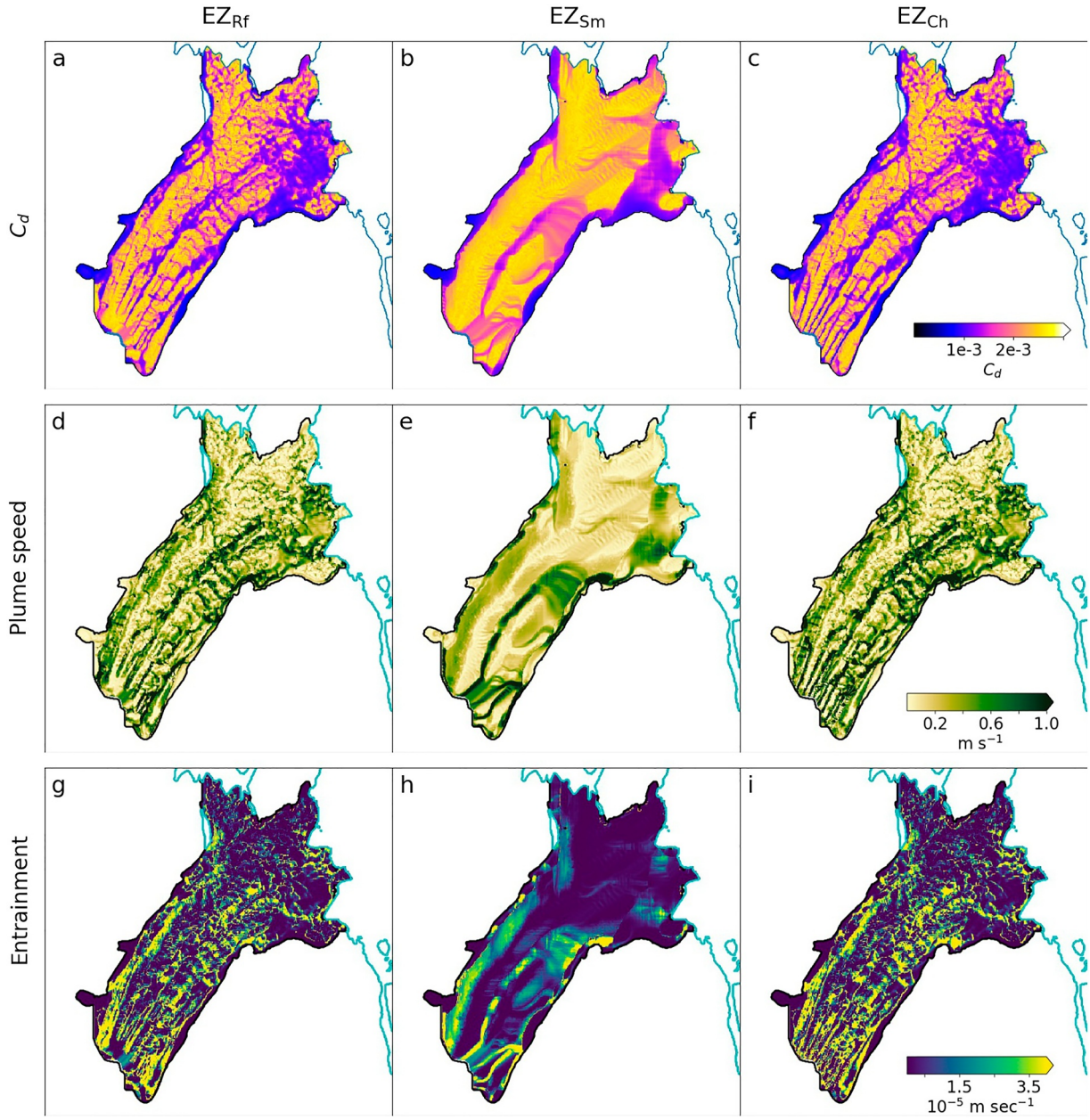

Figure 8. Comparison of different plume characteristics. The first row shows the computed drag coefficient (a–c), the second row displays plume speed (d–f), and the third row shows entrainment for three experiments with a grounding line discharge of 4.8 mSv (g–i). Each experiment utilizes a different ice base topography: Z_{Rf} (first column), Z_{Sm} (second column), and Z_{Ch} (third column).

hinge zone and shallower regions with access to warm ambient water near the grounding line cause higher entrainment compared to smooth ice base topographies.

The drainage of warm plume water into the channels results in a wider spread of plume water with high speed and thermal driving toward the middle of the domain. This in turn provides higher entrainment and more localized basal melting, and is not captured with smooth ice base topographies. Additionally, the *Reference* experiment failed to fully replicate the role of the channelized experiment in the hinge zone.

7. Summary and Conclusions

This study aimed to develop a numerical framework to investigate the plume water dynamics of 79NG and to assess the effects of key factors influencing the estimation of high-resolution basal melt rate, using a grid spacing of 150 m. Particular emphasis was placed on examining the effect of ice base topography roughness and incorporating the ice shelf's narrow basal channels in the hinge zone—features absent from standard ice thickness data sets. Experiments including basal channels closely replicate the observation-based spatial pattern of melt rates estimated by Wilson et al. (2017) and G. Wang et al. (2024). We also investigated the impact of subglacial discharge applying two different methods of forcing: discharge through channelized pathways and discharge evenly distributed along the grounding line. In addition, our study assessed the sensitivity of melt rates to discharge temperature.

In our experiments with glacial channels, we obtain simulated basal melt rates up to 150 m yr^{-1}, which compares well to the high melt rates observed near the grounding line by Zeising et al. (2024). The observation-based results and our simulations also both show that melt rates decreased with distance from the grounding line. Additionally, the application of the wet and dry algorithm, combined with the use of a variable drag coefficient—applied here for the first time in ice shelf plume models—is particularly valuable in the hinge zone. This is where previous plume modeling efforts have encountered numerical instability issues and where ice basal roughness is significantly higher than in other regions. These methods are crucial for accurately modeling low subglacial discharge seasons and for determining friction and turbulent exchange coefficients.

We found that using smooth ice base topographies to estimate basal melt rates not only significantly underestimated the spatial mean melt rate but also misrepresented the melt rate pattern. The discrepancies in the melt rate pattern are primarily attributed to plume water dynamics, influenced by ice base roughness. In the hinge zone of 79NG, introducing basal channels enhances the melt rate downstream of the hinge zone which improves agreement with observation-based estimates (Millan et al., 2023; G. Wang et al., 2024; Wilson et al., 2017). The plume water drains into the channels and flows downstream of the hinge zone, delivering more heat for melting in those regions. The resulting thicker plume within the channels reduces friction between the ice and water, allowing for higher plume speeds. This combination of increased heat supply and high flow speed leads to elevated melt rates near the grounding line and significantly greater lateral variability compared to experiments without channels. So far, these basal channels as observed by Zeising et al. (2024) are not incorporated in the standard ice thickness data sets such as Bedmachine (Morlighem et al., 2017b). We recommend adding these channels as it would improve models that need the ice shelf topography as an input.

Furthermore, our results show that subglacial discharge with temperature of 1.5°C increases melt rates and can further lead to melt rates larger than 100 m yr^{-1}. In cases of channelized discharge, large melt rates are localized but extend along the basal channels toward the middle of the ice shelf, whereas grounding line discharge results in a more uniform distribution of large melt rates. In all experiments, subglacial discharge increases the annual spatial mean melt rate near the grounding line to approximately three times the rate of increase numerically estimated for the entire ice shelf. The spatial mean melt rate in the calving zone remains largely unaffected by the discharge since the heat supplied by warm subglacial discharge dissipates. However, in the case of cold grounding line discharge, the spatial mean melt rate remains constant with increasing discharge across all the mentioned regions and the entire ice shelf. This occurs because cold subglacial discharge supplies less heat than warm subglacial discharge.

To conclude, this research demonstrates that resolving channelized systems in the hinge zone and small-scale features throughout the domain is crucial for ice shelves influenced by warm water. However, further investigation into utilizing an efficient plume model to develop and evaluate sub-grid scale topographic roughness parameterizations for coarse three-dimensional models would be valuable in mitigating the inability to capture small-scale features. Additionally, improving ice thickness data sets in the hinge zone is necessary. A realistic representation of subglacial discharge hydrology, along with consideration of time series for oceanic forcing, is highly recommended. Building on the success of approximating melt rates within our modeling framework, future work could also explore its application in coupled ocean-biogeochemical models to further advance studies of glacier-ocean interactions. Moreover, the developed plume model can easily be applied to other Greenland and Antarctic ice shelves.

Appendix A: Observed Basal Melt Rates

Figure A1 compares the observation-based estimates discussed in Section 6.1.

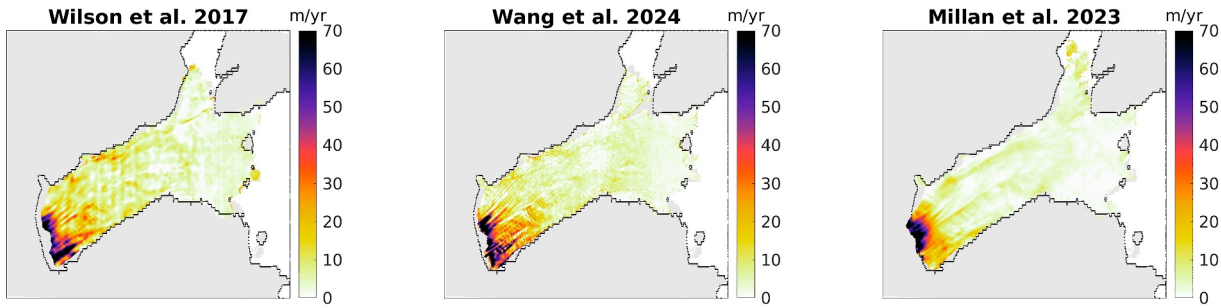

Figure A1. Averaged basal melt rates by Wilson et al. (2017), G. Wang et al. (2024), and Millan et al. (2023).

Data Availability Statement

The processed CTD profiles are sourced from the World Data Center PANGAEA (Kanzow et al., 2017). Ice sheet thickness and surface elevation data from the BedMachine Greenland v5 data set are obtained from the National Snow and Ice Data Center (Morlighem et al., 2017a). The data set from Mohammadi-Aragh (2024) includes model runs and analyses using GIPM (Mohammadi-Aragh & Burchard, 2024). Ice thickness data from the 2021 UWB survey are also sourced from the World Data Center PANGAEA (Zeising et al., 2023).

Acknowledgments

M.M.A., O.Z. M.R., and H.B. acknowledge the financial support by the German Federal Ministry for Education and Research (BMBF) in the framework of the GROCE project (Greenland Ice Sheet/Ocean Interaction, Grants 03F0778C and 03F0778A). K.K. and H.B. were supported by the Collaborative Research Centre TRR 181 on Energy Transfers in Atmosphere and Ocean funded by the German Research Foundation (Project 274762653). Data from airborne campaigns conducted by Alfred Wegener Institute (PRESURV79NG, 79NG-EC PI Humbert) were used within the BedMachine data set. We thank Xylar Asay-Davis, and three anonymous reviewers for their comments that improved this manuscript. We thank Nat Wilson and Chang-Qing Ke for providing basal melt rates of the 79NG derived from satellite imagery. We would also like to express our sincere thanks to Martin Losch and Sergey Danilov for their insightful discussions. Additionally, we extend our gratitude to Janin Schaffer for valuable contributions to the earlier version of this manuscript. We acknowledge support by the Open Access publication fund of Alfred-Wegener-Institut Helmholtz-Zentrum für Polar- und Meeresforschung. Open Access funding enabled and organized by Projekt DEAL.

References

Alley, K. E., Scambos, T. A., & Alley, R. B. (2022). The role of channelized basal melt in ice-shelf stability: Recent progress and future priorities. *Annals of Glaciology*, *63*(87–89), 18–22. https://doi.org/10.1017/aog.2023.5

Alley, K. E., Scambos, T. A., Alley, R. B., & Holschuh, N. (2019). Troughs developed in ice-stream shear margins precondition ice shelves for ocean-driven breakup. *Science Advances*, *5*(10), eaax2215. https://doi.org/10.1126/sciadv.aax2215

Alley, K. E., Scambos, T. A., Siegfried, M. R., & Fricker, H. A. (2016). Impacts of warm water on Antarctic ice shelf stability through basal channel formation. *Nature Geoscience*, *9*(4), 290–293. https://doi.org/10.1038/ngeo2675

Alley, R. B., Anandakrishnan, S., Christianson, K., Horgan, H. J., Muto, A., Parizek, B. R., et al. (2015). Oceanic forcing of ice-sheet retreat: West Antarctica and more. *Annual Review of Earth and Planetary Sciences*, *43*(1), 207–231. https://doi.org/10.1146/annurev-earth-060614-105344

Anhaus, P. (2017). *Circulation and ocean driven glacial melting in a Greenland fjord*. Masters dissertation. The University of Bergen.

Anselin, J., Holland, P., Jenkins, A., & Taylor, J. (2024). Ice base slope effects on the turbulent ice shelf-ocean boundary current. *Journal of Physical Oceanography*, *54*(7), 1545–1562. https://doi.org/10.1175/jpo-d-23-0256.1

Asay-Davis, X. S., Jourdain, N. C., & Nakayama, Y. (2017). Developments in simulating and parameterizing interactions between the Southern Ocean and the Antarctic ice sheet. *Current Climate Change Reports*, *3*(4), 316–329. https://doi.org/10.1007/s40641-017-0071-0

Beckmann, J., Perrette, M., & Ganopolski, A. (2018). Simple models for the simulation of submarine melt for a Greenland glacial system model. *The Cryosphere*, *12*(1), 301–323. https://doi.org/10.5194/tc-12-301-2018

Begeman, C. B., Asay-Davis, X., & Van Roekel, L. (2022). Ice-shelf ocean boundary layer dynamics from large-eddy simulations. *The Cryosphere*, *16*(1), 277–295. https://doi.org/10.5194/tc-16-277-2022

Beyer, S., Kleiner, T., Aizinger, V., Rückamp, M., & Humbert, A. (2018). A confined–unconfined aquifer model for subglacial hydrology and its application to the northeast Greenland ice stream. *The Cryosphere*, *12*(12), 3931–3947. https://doi.org/10.5194/tc-12-3931-2018

Burchard, H., Bolding, K., Jenkins, A., Losch, M., Reinert, M., & Umlauf, L. (2022). The vertical structure and entrainment of subglacial melt water plumes. *Journal of Advances in Modeling Earth Systems*, *14*(3), 1–34. https://doi.org/10.1029/2021ms002925

Cai, C., Rignot, E., Menemenlis, D., & Nakayama, Y. (2017). Observations and modeling of ocean-induced melt beneath Petermann Glacier ice shelf in northwestern Greenland. *Geophysical Research Letters*, *44*(16), 8396–8403. https://doi.org/10.1002/2017gl073711

Chartrand, A. M., & Howat, I. M. (2023). A comparison of contemporaneous airborne altimetry and ice-thickness measurements of Antarctic ice shelves. *Journal of Glaciology*, *69*(278), 1–14. https://doi.org/10.1017/jog.2023.49

Chartrand, A. M., Howat, I. M., Joughin, I. R., & Smith, B. E. (2024). Basal channels, ice thinning and grounding zone retreat at Thwaites Glacier, West Antarctica. *EGUsphere*, *2024*, 1–32.

Dinniman, M. S., Asay-Davis, X. S., Galton-Fenzi, B. K., Holland, P. R., Jenkins, A., & Timmermann, R. (2016). Modeling ice shelf/ocean interaction in Antarctica: A review. *Oceanography*, *29*(4), 144–153. https://doi.org/10.5670/oceanog.2016.106

Dow, C. F. (2022). The role of subglacial hydrology in Antarctic ice sheet dynamics and stability: A modelling perspective. *Annals of Glaciology*, *63*(87–89), 49–54. https://doi.org/10.1017/aog.2023.9

Dow, C. F., Lee, W. S., Greenbaum, J. S., Greene, C. A., Blankenship, D. D., Poinar, K., et al. (2018). Basal channels drive active surface hydrology and transverse ice shelf fracture. *Science Advances*, *4*(6), eaao7212. https://doi.org/10.1126/sciadv.aao7212

Dutrieux, P., Vaughan, D. G., Corr, H. F., Jenkins, A., Holland, P. R., Joughin, I., & Fleming, A. (2013). Pine island glacier ice shelf melt distributed at kilometre scales. *The Cryosphere*, *7*(5), 1543–1555. https://doi.org/10.5194/tc-7-1543-2013

Ebert, E. E. (2009). Neighborhood verification: A strategy for rewarding close forecasts. *Weather and Forecasting*, *24*(6), 1498–1510. https://doi.org/10.1175/2009waf2222251.1

Gayen, B., Griffiths, R. W., & Kerr, R. C. (2015). Melting driven convection at the ice-seawater interface. *Procedia IUTAM*, *15*, 78–85. https://doi.org/10.1016/j.piutam.2015.04.012

Gladish, C. V., Holland, D. M., Holland, P. R., & Price, S. F. (2012). Ice-shelf basal channels in a coupled ice/ocean model. *Journal of Glaciology*, *58*(212), 1227–1244. https://doi.org/10.3189/2012jog12j003

Gwyther, D. E., Galton-Fenzi, B. K., Dinniman, M. S., Roberts, J. L., & Hunter, J. R. (2015). The effect of basal friction on melting and freezing in ice shelf–ocean models. *Ocean Modelling*, *95*, 38–52. https://doi.org/10.1016/j.ocemod.2015.09.004

Hellmer, H. H., & Olbers, D. J. (1989). A two-dimensional model for the thermohaline circulation under an ice shelf. *Antarctic Science*, *1*(4), 325–336. https://doi.org/10.1017/s0954102089000490

Hill, E. A., Carr, J. R., & Stokes, C. R. (2017). A review of recent changes in major marine-terminating outlet glaciers in Northern Greenland. *Frontiers in Earth Science*, *4*, 111. https://doi.org/10.3389/feart.2016.00111

Hoffman, M. J., Asay-Davis, X., Price, S. F., Fyke, J., & Perego, M. (2019). Effect of subshelf melt variability on sea level rise contribution from Thwaites Glacier, Antarctica. *Journal of Geophysical Research: Earth Surface*, *124*(12), 2798–2822. https://doi.org/10.1029/2019jf005155

Holland, D. M., & Jenkins, A. (1999). Modeling thermodynamic ice–ocean interactions at the base of an ice shelf. *Journal of Physical Oceanography*, *29*(8), 1787–1800. https://doi.org/10.1175/1520-0485(1999)029<1787:mtioia>2.0.co;2

Holland, P. R., Corr, H. F., Vaughan, D. G., Jenkins, A., & Skvarca, P. (2009). Marine ice in Larsen ice shelf. *Geophysical Research Letters*, *36*(11), L11604. https://doi.org/10.1029/2009gl038162

Holland, & Feltham, D. L. (2006). The effects of rotation and ice shelf topography on frazil-laden ice shelf water plumes. *Journal of Physical Oceanography*, *36*(12), 2312–2327. https://doi.org/10.1175/jpo2970.1

Humbert, A., Helm, V., Neckel, N., Zeising, O., Rückamp, M., Khan, S. A., et al. (2023). Precursor of disintegration of Greenland's largest floating ice tongue. *The Cryosphere*, *17*(7), 2851–2870. https://doi.org/10.5194/tc-17-2851-2023

Jenkins, A. (1991). A one-dimensional model of ice shelf-ocean interaction. *Journal of Geophysical Research*, *96*(C11), 20671–20677. https://doi.org/10.1029/91jc01842

Jenkins, A. (2011). Convection-driven melting near the grounding lines of ice shelves and tidewater glaciers. *Journal of Physical Oceanography*, *41*(12), 2279–2294. https://doi.org/10.1175/jpo-d-11-03.1

Jenkins, A., Nicholls, K. W., & Corr, H. F. (2010). Observation and parameterization of ablation at the base of Ronne Ice Shelf, Antarctica. *Journal of Physical Oceanography*, *40*(10), 2298–2312. https://doi.org/10.1175/2010jpo4317.1

Jungclaus, J. H., & Backhaus, J. O. (1994). Application of a transient reduced gravity plume model to the Denmark Strait Overflow. *Journal of Geophysical Research*, *99*(C6), 12375–12396. https://doi.org/10.1029/94jc00528

Kanzow, T., Humbert, A., Mölg, T., Scheinert, M., Braun, M., Burchard, H., et al. (2025). The system of atmosphere, land, ice and ocean in the region near the 79N Glacier in northeast Greenland: Synthesis and key findings from the Greenland Ice Sheet–Ocean Interaction (GROCE) experiment. *The Cryosphere*, *19*(5), 1789–1824. https://doi.org/10.5194/tc-19-1789-2025

Kanzow, T., von Appen, W.-J., Schaffer, J., Köhn, E., Tsubouchi, T., Wilson, N., & Wisotzki, A. (2017). Physical oceanography measured with CTD/Large volume Watersampler-system during POLARSTERN cruise PS100 (ARK-XXX/2) [Dataset]. *PANGAEA*. https://doi.org/10.1594/PANGAEA.871025

Klingbeil, K., Mohammadi-Aragh, M., Gräwe, U., & Burchard, H. (2014). Quantification of spurious dissipation and mixing–Discrete variance decay in a Finite-Volume framework. *Ocean Modelling*, *81*, 49–64. https://doi.org/10.1016/j.ocemod.2014.06.001

Kochergin, V. (1987). Three-dimensional prognostic models. *Three-Dimensional Coastal Ocean Models*, *4*, 201–208. https://doi.org/10.1029/co004p0201

Lambert, E., Jüling, A., Van De Wal, R. S., & Holland, P. R. (2023). Modelling Antarctic ice shelf basal melt patterns using the one-layer Antarctic model for dynamical downscaling of ice-ocean exchanges (laddie v1. 0). *The Cryosphere*, *17*(8), 3203–3228.

Larter, R. D. (2022). Basal melting, roughness and structural integrity of ice shelves. *Geophysical Research Letters*, *49*(4), e2021GL097421. https://doi.org/10.1029/2021gl097421

Lazeroms, W. M., Jenkins, A., Gudmundsson, G. H., & Van De Wal, R. S. (2018). Modelling present-day basal melt rates for Antarctic ice shelves using a parametrization of buoyant meltwater plumes. *The Cryosphere*, *12*(1), 49–70. https://doi.org/10.5194/tc-12-49-2018

Le Brocq, A. M., Ross, N., Griggs, J. A., Bingham, R. G., Corr, H. F., Ferraccioli, F., et al. (2013). Evidence from ice shelves for channelized meltwater flow beneath the Antarctic Ice Sheet. *Nature Geoscience*, *6*(11), 945–948. https://doi.org/10.1038/ngeo1977

Lilien, D. A., Joughin, I., Smith, B., & Gourmelen, N. (2019). Melt at grounding line controls observed and future retreat of Smith, Pope, and Kohler Glaciers. *The Cryosphere*, *13*(11), 2817–2834. https://doi.org/10.5194/tc-13-2817-2019

Lindeman, M. R., Straneo, F., Wilson, N. J., Toole, J. M., Krishfield, R. A., Beaird, N. L., et al. (2020). Ocean circulation and variability beneath nioghalvfjerdsbræ (79 North Glacier) ice tongue. *Journal of Geophysical Research: Oceans*, *125*(8), e2020JC016091. https://doi.org/10.1029/2020jc016091

Losch, M. (2008). Modeling ice shelf cavities in a z coordinate ocean general circulation model. *Journal of Geophysical Research*, *113*(C8), C08043. https://doi.org/10.1029/2007jc004368

Malyarenko, A., Wells, A. J., Langhorne, P. J., Robinson, N. J., Williams, M. J., & Nicholls, K. W. (2020). A synthesis of thermodynamic ablation at ice–ocean interfaces from theory, observations and models. *Ocean Modelling*, *154*, 101692. https://doi.org/10.1016/j.ocemod.2020.101692

Mayer, C., Reeh, N., Jung-Rothenhäusler, F., Huybrechts, P., & Oerter, H. (2000). The subglacial cavity and implied dynamics under Nioghalvfjerdsfjorden Glacier, NE-Greenland. *Geophysical Research Letters*, *27*(15), 2289–2292. https://doi.org/10.1029/2000gl011514

Mayer, C., Schaffer, J., Hattermann, T., Floricioiu, D., Krieger, L., Dodd, P. A., et al. (2018). Large ice loss variability at Nioghalvfjerdsfjorden Glacier, Northeast-Greenland. *Nature Communications*, *9*(1), 1–11. https://doi.org/10.1038/s41467-018-05180-x

McPherson, R. A., Wekerle, C., Kanzow, T., Ionita, M., Heukamp, F. O., Zeising, O., & Humbert, A. (2024). Atmospheric blocking slows ocean-driven melting of Greenland's largest glacier tongue. *Science*, *385*(6715), 1360–1366. https://doi.org/10.1126/science.ado5008

Mellor, G., & Durbin, P. (1975). The structure and dynamics of the ocean surface mixed layer. *Journal of Physical Oceanography*, *5*(4), 718–728. https://doi.org/10.1175/1520-0485(1975)005<0718:tsadot>2.0.co;2

Millan, R., Jager, E., Mouginot, J., Wood, M. H., Larsen, S. H., Mathiot, P., et al. (2023). Rapid disintegration and weakening of ice shelves in North Greenland. *Nature Communications*, *14*(1), 6914. https://doi.org/10.1038/s41467-023-42198-2

Millgate, T., Holland, P. R., Jenkins, A., & Johnson, H. L. (2013). The effect of basal channels on oceanic ice-shelf melting. *Journal of Geophysical Research: Oceans*, *118*(12), 6951–6964. https://doi.org/10.1002/2013jc009402

Mohammadi-Aragh, M. (2024). Supplementary data for the publication: "Impact of ice topography, basal channels and subglacial discharge on basal melting under the floating ice tongue of 79N Glacier, northeast Greenland". *Zenodo*. https://doi.org/10.5281/zenodo.13831183

Mohammadi-Aragh, M., & Burchard, H. (2024). Source code for the general ice shelf water plume model (GIPM). https://doi.org/10.5281/zenodo.4716817

Mohammadi-Aragh, M., Klingbeil, K., Brüggemann, N., Eden, C., & Burchard, H. (2015). The impact of advection schemes on restratifiction due to lateral shear and baroclinic instabilities. *Ocean Modelling*, *94*, 112–127. https://doi.org/10.1016/j.ocemod.2015.07.021

Mohammadi-Aragh, M., Losch, M., & Goessling, H. F. (2020). Comparing Arctic sea ice model simulations to satellite observations by multiscale directional analysis of linear kinematic features. *Monthly Weather Review*, *148*(8), 3287–3303. https://doi.org/10.1175/mwr-d-19-0359.1

Morlighem, M., Williams, C. N., Rignot, E., An, L., Arndt, J. E., Bamber, J. L., et al. (2017a). BedMachine v3: Complete bed topography and ocean bathymetry mapping of Greenland from multibeam echo sounding combined with mass conservation. *Geophysical Research Letters*, *44*(21), 11–051. https://doi.org/10.1002/2017gl074954

Morlighem, M., Williams, C. N., Rignot, E., An, L., Arndt, J. E., Bamber, J. L., et al. (2017b). *IceBridge BedMachine Greenland, version 3. Boulder, Colorado USA*. NASA National Snow and Ice Data Center Distributed Active Archive Center. https://doi.org/10.5067/2CIX82HUV88Y

Nakayama, Y., Cai, C., & Seroussi, H. (2021). Impact of subglacial freshwater discharge on pine island ice shelf. *Geophysical Research Letters*, *48*(18), e2021GL093923. https://doi.org/10.1029/2021gl093923

Narkevic, A., Csatho, B., & Schenk, T. (2023). Rapid basal channel growth beneath Greenland's longest floating ice shelf. *Geophysical Research Letters*, *50*(11), e2023GL103226. https://doi.org/10.1029/2023gl103226

Neckel, N., Zeising, O., Steinhage, D., Helm, V., & Humbert, A. (2020). Seasonal observations at 79°N Glacier (Greenland) from remote sensing and in situ measurements. *Frontiers in Earth Science*, *8*, 142. https://doi.org/10.3389/feart.2020.00142

Nienow, P., Sole, A., Slater, D. A., & Cowton, T. (2017). Recent advances in our understanding of the role of meltwater in the Greenland ice sheet system. *Current Climate Change Reports*, *3*(4), 330–344. https://doi.org/10.1007/s40641-017-0083-9

Payne, A. J., Holland, P. R., Shepherd, A. P., Rutt, I. C., Jenkins, A., & Joughin, I. (2007). Numerical modeling of ocean-ice interactions under Pine Island Bay's ice shelf. *Journal of Geophysical Research*, *112*(C10), C10019. https://doi.org/10.1029/2006jc003733

Purich, A. (2022). How the ocean melts Antarctic ice. *Communications Earth & Environment*, *3*(1), 1–3. https://doi.org/10.1038/s43247-022-00471-0

Reinert, M., Lorenz, M., Klingbeil, K., Büchmann, B., & Burchard, H. (2023). High-resolution simulations of the plume dynamics in an idealized 79°N glacier cavity using adaptive vertical coordinates. *Journal of Advances in Modeling Earth Systems*, *15*(10), e2023MS003721. https://doi.org/10.1029/2023ms003721

Rignot, E., & Steffen, K. (2008). Channelized bottom melting and stability of floating ice shelves. *Geophysical Research Letters*, *35*(2), L02503. https://doi.org/10.1029/2007gl031765

Scambos, T. A., Bell, R. E., Alley, R. B., Anandakrishnan, S., Bromwich, D., Brunt, K., et al. (2017). How much, how fast? A science review and outlook for research on the instability of Antarctica's Thwaites glacier in the 21st century. *Global and Planetary Change*, *153*, 16–34. https://doi.org/10.1016/j.gloplacha.2017.04.008

Schaffer, J., Kanzow, T., von Appen, W.-J., von Albedyll, L., Arndt, J. E., & Roberts, D. H. (2020). Bathymetry constrains ocean heat supply to Greenland's largest glacier tongue. *Nature Geoscience*, *13*(3), 227–231. https://doi.org/10.1038/s41561-019-0529-x

Schaffer, J., von Appen, W.-J., Dodd, P. A., Hofstede, C., Mayer, C., de Steur, L., & Kanzow, T. (2017). Warm water pathways toward Nioghalvfjerdsfjorden Glacier, Northeast Greenland. *Journal of Geophysical Research: Oceans*, *122*(5), 4004–4020. https://doi.org/10.1002/2016JC012462

Seroussi, H., Morlighem, M., Rignot, E., Larour, E., Aubry, D., Ben Dhia, H., & Kristensen, S. S. (2011). Ice flux divergence anomalies on 79North glacier, Greenland. *Geophysical Research Letters*, *38*(9), L09501. https://doi.org/10.1029/2011gl047338

Sikirić, M. D., Janeković, I., & Kuzmić, M. (2009). A new approach to bathymetry smoothing in sigma-coordinate ocean models. *Ocean Modelling*, *29*(2), 128–136. https://doi.org/10.1016/j.ocemod.2009.03.009

Sugiyama, S., Skvarca, P., Naito, N., Enomoto, H., Tsutaki, S., Tone, K., et al. (2011). Ice speed of a calving glacier modulated by small fluctuations in basal water pressure. *Nature Geoscience*, *4*(9), 597–600. https://doi.org/10.1038/ngeo1218

Vaughan, D. G., Corr, H. F., Bindschadler, R. A., Dutrieux, P., Gudmundsson, G. H., Jenkins, A., et al. (2012). Subglacial melt channels and fracture in the floating part of pine island glacier, Antarctica. *Journal of Geophysical Research*, *117*(F3), F03012. https://doi.org/10.1029/2012jf002360

Vijay, S., Khan, S. A., Kusk, A., Solgaard, A. M., Moon, T., & Bjørk, A. A. (2019). Resolving seasonal ice velocity of 45 Greenlandic glaciers with very high temporal details. *Geophysical Research Letters*, *46*(3), 1485–1495. https://doi.org/10.1029/2018gl081503

Walker, R., Dupont, T., Parizek, B., & Alley, R. (2008). Effects of basal-melting distribution on the retreat of ice-shelf grounding lines. *Geophysical Research Letters*, *35*(17), L17503. https://doi.org/10.1029/2008gl034947

Wang, G., Ke, C., Fan, Y., Shen, X., Nourani, V., Sankaran, A., et al. (2024). Accelerated basal melt rates of ice shelves in North Greenland from 2013 to 2022 estimated with the high-resolution ArcticDEM. *Journal of Geophysical Research: Oceans*, *129*(12), e2024JC021509. https://doi.org/10.1029/2024jc021509

Wang, Z., Song, X., Zhang, B., Liu, T., & Geng, H. (2020). Basal channel extraction and variation analysis of Nioghalvfjerdsfjorden ice Shelf in Greenland. *Remote Sensing*, *12*(9), 1474. https://doi.org/10.3390/rs12091474

Washam, P., Nicholls, K. W., Münchow, A., & Padman, L. (2019). Summer surface melt thins Petermann Gletscher Ice shelf by enhancing channelized basal melt. *Journal of Glaciology*, *65*(252), 662–674. https://doi.org/10.1017/jog.2019.43

Weertman, J. (1957). Deformation of floating ice shelves. *Journal of Glaciology*, *3*(21), 38–42. https://doi.org/10.3189/s0022143000024710

Wekerle, C., McPherson, R., von Appen, W.-J., Wang, Q., Timmermann, R., Scholz, P., et al. (2024). Atlantic water warming increases melt below northeast Greenland's last floating ice tongue. *Nature Communications*, *15*(1), 1336. https://doi.org/10.1038/s41467-024-45650-z

Wilson, N., & Straneo, F. (2015). Water exchange between the continental shelf and the cavity beneath Nioghalvfjerdsbræ (79 North Glacier). *Geophysical Research Letters*, *42*(18), 7648–7654. https://doi.org/10.1002/2015gl064944

Wilson, N., Straneo, F., & Heimbach, P. (2017). Satellite-derived submarine melt rates and mass balance (2011-2015) for Greenland's largest remaining ice tongues. *The Cryosphere*, *11*(6), 2773–2782. https://doi.org/10.5194/tc-11-2773-2017

Zalesny, V., & Ivchenko, V. (2010). Modeling the global circulation response and the regional response of the Arctic Ocean to the external forcing anomalies. *Oceanology*, *50*(6), 829–840. https://doi.org/10.1134/s0001437010060020

Zeising, O., Helm, V., Gupta, A., Steinhage, D., & Humbert, A. (2023). Ice surface elevation and ice thickness at 79°N Glacier, Greenland from airborne measurements in July 2021 [Dataset]. *PANGAEA*. https://doi.org/10.1594/PANGAEA.963752

Zeising, O., Neckel, N., Dörr, N., Helm, V., Steinhage, D., Timmermann, R., & Humbert, A. (2024). Extreme melting at Greenland's largest floating ice tongue. *The Cryosphere*, *18*(3), 1333–1357. https://doi.org/10.5194/tc-18-1333-2024

Zhao, K. X., Skyllingstad, E. D., & Nash, J. D. (2024). Improved parameterizations of vertical ice-ocean boundary layers and melt rates. *Geophysical Research Letters*, *51*(4), e2023GL105862. https://doi.org/10.1029/2023gl105862